Geophysical Journal International

Geophys. J. Int. (2016) **207,** 901–933
Advance Access publication 2016 August 15
GJI Seismology

doi: 10.1093/gji/ggw309

Azimuthal seismic anisotropy in the Earth's upper mantle and the thickness of tectonic plates

A.J. Schaeffer,[1,2] S. Lebedev[2] and T.W. Becker[3]

[1] *Department of Earth and Environmental Sciences, University of Ottawa, Ottawa K1N 6N5, Canada. E-mail: andrew.schaeffer@uottawa.ca*
[2] *Geophysics Section, School of Cosmic Physics, Dublin Institute for Advanced Studies, Dublin, Ireland*
[3] *Jackson School of Geosciences, University of Texas at Austin, Austin, TX 78712, USA*

Accepted 2016 August 11. Received 2016 July 26; in original form 2016 January 12

SUMMARY

Azimuthal seismic anisotropy, the dependence of seismic wave speeds on propagation azimuth, is largely due to fabrics within the Earth's crust and mantle, produced by deformation. It thus provides constraints on the distribution and evolution of deformation within the upper mantle. Here, we present a new global, azimuthally anisotropic model of the crust, upper mantle and transition zone. Two versions of this new model are computed: the rough SL2016svAr and the smooth SL2016svA. Both are constrained by a very large data set of waveform fits (∼750 000 vertical component seismogram fits). Automated, multimode waveform inversion was used to extract structural information from surface and *S* wave forms in broad period ranges (dominantly from 11 to 450 s, with the best global sampling in the 20–350 s range), yielding resolving power from the crust down to the transition zone. In our global tomographic inversion, regularization of anisotropy is implemented to more uniformly recover the amplitude and orientation of anisotropy, including near the poles. Our massive waveform data set, with complementary large global networks and high-density regional array data, produces improved resolution of global azimuthal anisotropy patterns. We show that regional scale variations, related to regional lithospheric deformation and mantle flow, can now be resolved by the global models, in particular in densely sampled regions. For oceanic regions, we compare quantitatively the directions of past and present plate motions and the fast-propagation orientations of anisotropy. By doing so, we infer the depth of the boundary between the rigid, high-viscosity lithosphere (preserving ancient, frozen fabric) and the rheologically weak asthenosphere (characterized by fabric developed recently). The average depth of thus inferred rheological lithosphere-asthenosphere boundary (LAB) beneath the world's oceans is ∼115 km. The LAB depth displays a clear dependence on the age of the oceanic lithosphere, closely matching the 1200 °C half-space cooling isotherm for all oceanic ages. In continental regions, azimuthal anisotropy is characterized by smaller-scale 3-D variations. Quantitative comparisons of the tomographic models with global *SKS* splitting measurements confirm the basic agreement of the two types of anisotropy analysis; they also offer a new insight into the average rheological thickness of continental lithosphere. In spite of significant recent improvements in the resolution of upper-mantle anisotropic structure, correlations between the anisotropic components of current global tomographic models remain much lower than between the isotropic ones. Our comparisons of the current models show which features are resolved consistently by different models, and therefore provide a means to estimate the robustness of anisotropic patterns and amplitudes. Significantly lower correlations are observed at depths greater than ∼300 km, compared to those shallower, which suggests that global azimuthal anisotropy models are yet to reach consensus on the nature of anisotropy in the transition zone.

Key words: Inverse theory; Mantle processes; Surface waves and free oscillations; Seismic anisotropy; Seismic tomography; Dynamics of lithosphere and mantle.

1 INTRODUCTION

Deformation within the Earth gives rise to seismic anisotropy, both through crystallographic preferred orientation (CPO, also referred to as lattice preferred orientation, LPO) of natively anisotropic minerals, and through shape preferred orientation (SPO), such as that of pockets of partial melt or pervasive cracks (Montagner & Guillot 2002; Long & Becker 2010). In the upper mantle, the volumetrically dominant mineral olivine likely represents the primary source of observed anisotropy due to its large single-crystal shear wave anisotropy (∼18 per cent; Mainprice 2007); other moderate constituents (by volume) as such as orthopyroxene and clinopyroxene are also anisotropic (≥10 per cent; Anderson 1989; Babuska & Cara 1991), and much smaller contributions from garnet (Montagner & Guillot 2002).

The anisotropy of a mantle rock depends on its constituent minerals and the relative orientation of their crystallographic axes. When deformed in the dislocation creep regime under simple shear, an olivine aggregate will develop an LPO with the fast axis dominantly aligning with the direction of maximum shear (Karato *et al.* 2008). For example, the pyrolite model for the upper mantle has been proposed to have a maximum anisotropy of ∼3–4 per cent (Montagner & Anderson 1989).

Seismic anisotropy represents a record of deformation within the Earth. It thus offers insights into the dynamics of the mantle and crust. Measurements of seismic anisotropy span a broad range in scale-lengths: from local seismometer-proximal results (obtained, e.g. from shear wave splitting) to regional and global-scale studies employing surface and body waves, as well as regional-scale measurements of P_n and S_n phases.

Global, 3-D seismic tomography models capture the lateral variations and depth dependence of the strength and orientation of the anisotropic fast-propagation direction. In recent years, these models have improved in terms of their spatial resolution, enabling more detailed investigation of the coupling between the lithosphere and the underlying mantle, beneath both continents and oceans. For instance, layering of azimuthal anisotropy has been documented within the lithosphere and asthenosphere around the world (e.g. Simons *et al.* 2002; Debayle *et al.* 2005; Marone *et al.* 2007; Lebedev & van der Hilst 2008; Ekström 2011; Yuan *et al.* 2011; Debayle & Ricard 2013; Yuan & Beghein 2013; Becker *et al.* 2014; Beghein *et al.* 2014; Burgos *et al.* 2014; Debayle *et al.* 2016). With the recent emergence of large-scale dense arrays of broad-band instruments, the mapping of the 3-D distribution of anisotropy has been performed with increasingly higher resolution (e.g. Yang & Forsyth 2006; Yao *et al.* 2006; Zhang *et al.* 2007; Deschamps *et al.* 2008a,b; Lin *et al.* 2010; Ekström 2011; Roux *et al.* 2011; Yuan *et al.* 2011; Sodoudi *et al.* 2013; Zhu & Tromp 2013; Pandey *et al.* 2015), now approaching the resolution needed for determination of the dynamics of continental deformation.

Quantitative comparisons between different seismic tomography models have demonstrated that isotropic structures are significantly better resolved than anisotropic features, as evidenced by high correlations of recent models for wavelengths of thousands to several hundreds of kilometres (Becker & Boschi 2002; Meschede & Romanowicz 2015; Schaeffer & Lebedev 2015; Debayle *et al.* 2016). The anisotropic components, in contrast, have shown much lower agreement between models (Becker *et al.* 2007; Kustowski *et al.* 2008; Moulik & Ekstrom 2014; Chang *et al.* 2015).

In the last decade, the rapid growth in global seismic instrumentation, combined with the implementation of automated methods, have enabled the generation of a variety of global and continental-scale anisotropic tomography models (e.g. Lebedev & van der Hilst 2008; Becker *et al.* 2012; Debayle & Ricard 2012; Debayle & Ricard 2013; French *et al.* 2013; Schaeffer & Lebedev 2013; Yuan & Beghein 2013; Auer *et al.* 2014; Burgos *et al.* 2014; Chang *et al.* 2014; Moulik & Ekstrom 2014; Schaeffer & Lebedev 2014; Yuan & Beghein 2014; Debayle *et al.* 2016). The increased data redundancy enables significantly improved resolving power at different scales. The convergence of data sampling between different anisotropic tomography models is expected to not only improve their relative correlation across a range of spatial wavelengths, but also provide insight into the structures and processes that they most robustly constrain.

In this paper, we present a pair of global, azimuthally anisotropic shear-velocity models, constrained by a very large vertical-component seismogram data set, all successfully fit using the Automated Multimode Inversion (AMI; Lebedev *et al.* 2005) of surface and *S* waveforms. The first model, SL2016svA, is smoother, targeting the longer wavelength features in the upper mantle, which is accomplished through relatively strong regularization of the tomographic inversion, enforcing laterally smooth variations. The second model, SL2016svAr, is less smooth and targets higher resolution, in particular, in well-sampled continental regions.

We begin by briefly outlining the data set, methods and the regularization of the inversion, which has to be more elaborate for anisotropic perturbations compared to isotropic ones. We then discuss and quantitatively compare our models with four recently published global tomographic models of azimuthal anisotropy in the upper mantle, as well as with a global spherical harmonic expansion of *SKS* splitting measurements. Next, we use these two new models to examine anisotropic fabrics within continental and oceanic regions. Lastly, we evaluate the thickness of tectonic plates based on the orientation of azimuthal seismic anisotropy with respect to plate motions. We also discuss the reliability of current anisotropic tomography models in the deep upper mantle and transition zone.

2 DATA AND METHODS

The two shear wave, azimuthal anisotropy models presented in this paper, SL2016svA and SL2016svAr, are constructed using the same waveform inversion methods and the same data set as the isotropic shear wave model SL2013sv (Schaeffer & Lebedev 2013). (We note that the model SL2016svA has previously been utilized by Becker *et al.* (2014) and Becker *et al.* (2015), where it was referred to by a tentative name SL2013svA.) In this section, we include a brief description of the data set and a summary of our multimode surface waveform tomography methods (for a complete description see Lebedev *et al.* 2005; Lebedev & van der Hilst 2008; Schaeffer & Lebedev 2013).

The complete data set consists of ∼750 000 successfully fit, vertical component broad-band displacement seismograms recorded at 3383 broad-band stations of international, national, regional and temporary networks operating between 1994 and 2012. This corresponds to 24 628 events selected from those within the global Centroid Moment Tensor (CMT) catalogue (e.g. Ekström *et al.* 2012). The data set covers the broad period range dominantly between 20 and 350 s, with some measurements extending down to 12 s and up to 450 s (see fig. B2 in Schaeffer & Lebedev 2013). These stations and events are plotted in Fig. 1. From the initial set of waveform fits, a subset of ∼522 000 most mutually consistent fits were selected, using outlier analysis as described in Schaeffer & Lebedev (2013). The culling of the initial data set exploited its redundancy

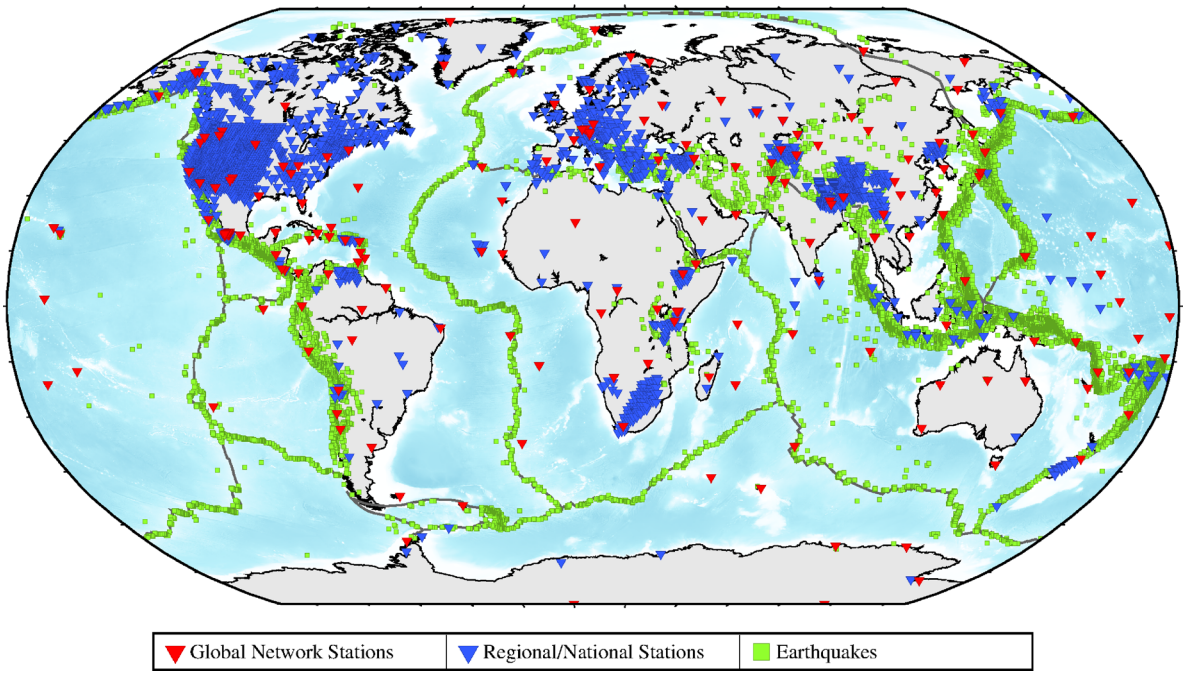

Figure 1. The 3833 stations of global and international networks (red triangles) and of national, regional and temporary networks (blue triangles) and the 24 628 events from the global centroid moment tensor catalogue (e.g. Ekström *et al.* 2012) (green squares), used in the tomography.

in order to remove the data with the largest errors (primarily due to errors in source locations, origin times and mechanisms, timing at the stations, and inaccurate response information).

The inversion procedure is split into three main steps. First, we perform the Automated Multimode Inversion (AMI; Lebedev *et al.* 2005) of our data set of pre-processed (filtered, response corrected and quality-controlled) vertical component broad-band displacement seismograms. This initial data set, consisting of several millions of seismograms, includes numerous small events recorded at long distances; those of them with low signal-to-noise ratios are rejected swiftly by the waveform inversion algorithm. AMI enables the processing of very large seismic data sets through its automated processing, enforcement of strict data-synthetic misfit criteria across a set of time-frequency windows, selected on a case-by-case basis, and elaborate phase weights. The result of the waveform inversion of each seismogram is a set of linear equations with uncorrelated uncertainties (Nolet 1990) that describes 1-D average perturbations in *S*- and *P*-wave velocity with respect to a 3-D reference model within approximate sensitivity volumes between the source and receiver pair (Lebedev & van der Hilst 2008).

In the second step, the equations generated by AMI for all the successfully fit seismograms are combined together into a single, very large system and solved for the 3-D distributions of *P* and *S* velocities, and 2Ψ *S*-wave azimuthal anisotropy, as a function of depth, spanning from the crust through the upper mantle and transition zone, and to the upper part of the lower mantle. The inversion is carried out subject to regularization, in the form of lateral smoothing and gradient damping, vertical gradient damping, and relatively minor norm damping. The third step consists of outlier analysis of the data set (Lebedev & van der Hilst 2008; Schaeffer & Lebedev 2013), set up so as to select *a posteriori* the most mutually consistent equations to be re-inverted for the final model.

The models are parametrized laterally using a global triangular grid of knots (Wang & Dahlen 1995). Vertically, each model is parametrized using triangular basis functions centred at 7, 20, 36, 56, 80, 110, 150, 200, 260, 330, 410-, 410+, 485, 585, 660-, 660+, 810 and 1009 km depth (note that transition zone discontinuities utilize pairs of half triangles). Examples of the parametrizations are presented in fig. 4 of Lebedev & van der Hilst (2008) and fig. 5 of Schaeffer & Lebedev (2013). Path re-weighting (Lebedev & van der Hilst 2008) is performed in order to reduce the effect of commonly sampled paths dominating the data set. Both AMI and the tomographic inversion utilize the same 3-D reference model. The model consists of a 3-D crustal model based on a smoothed version of Crust2 (Bassin *et al.* 2000), augmented with global topographic and bathymetric databases. Underlying the Moho (fixed to that of Crust2), we used a (substantially) modified AK135 (Kennett *et al.* 1995), as in Schaeffer & Lebedev (2013), recomputed at a reference period of 50 s, approximately in the middle of the waveform inversion period range.

In the following section, we outline the parametrization of anisotropy in the inversion, and provide greater detail in the Appendix.

3 ANISOTROPIC PARAMETRIZATION

Surface wave azimuthal anisotropy in a smoothly varying medium is commonly expressed as small perturbations from the isotropic velocity given by a series of π-periodic and $\pi/2$-periodic terms (Smith & Dahlen 1973):

$$\begin{aligned} C(\omega, \Psi, \theta, \phi) \;=\; & A_0(\omega, \theta, \phi) \\ & + A_1(\omega, \theta, \phi)\cos 2\Psi + A_2(\omega, \theta, \phi)\sin 2\Psi \\ & + A_3(\omega, \theta, \phi)\cos 4\Psi + A_4(\omega, \theta, \phi)\sin 4\Psi, \quad (1) \end{aligned}$$

where $C(\omega, \Psi, \theta, \phi)$ is the phase velocity at the azimuth Ψ (measured with respect to the local meridian), $A_0(\omega, \theta, \phi)$ is the isotropic-average phase speed, (A_1, A_2) and (A_3, A_4) are the coefficients for the π-periodic and $\pi/2$-periodic azimuthal variations, respectively, ω is the angular frequency, θ is the longitude and ϕ is the latitude. In the vertically polarized *S*-wave models (constrained by Rayleigh-wave

fundamental and higher modes) that we present in this work, we focus on the π-periodic ('2Ψ') azimuthal anisotropy, and therefore only retain the A_0, A_1 and A_2 terms of the expansion. Such simplifications have been previously justified for the separate analysis of Rayleigh and Love waves focussed on the upper mantle, with the Love wave anisotropy pattern, in contrast to Rayleigh waves, dominated by the $\pi/2$-periodic ('4Ψ') terms A_3 and A_4 (e.g. Montagner & Tanimoto 1991; Trampert & Woodhouse 2003; Ekström 2011; Adam & Lebedev 2012). (We note that for short-period Rayleigh waves sampling the continental crust, there are also indications for non-negligible 4Ψ terms, in addition to the 2Ψ ones (Adam & Lebedev 2012; Polat *et al.* 2012).)

Our implementation (Lebedev & van der Hilst 2008) projects the parameter pairs (A_1, A_2) as vectors onto a geographical coordinate system. As a result, cosine terms represent the north–south component of azimuthal anisotropy and sine terms the east–west components. This formulation leads to a linear inverse problem for the spatial distribution of the parameters $A_i(r, \theta, \phi)$.

The model is parametrized laterally on a triangular grid of knots (Wang & Dahlen 1995), with an approximately equal interknot spacing. This local parametrization enables easy co-registration of different resolution grids, and as a result makes it simple to transform from one to another. This is important as we utilize a dense grid (∼28 km spacing) for integrating the reference model and sensitivity kernels, and a coarser model grid on which the 3-D variations in seismic velocity are solved. In Appendix A1, we detail the method by which the sensitivity kernels are mapped onto the integration and model grids.

The inversion is parametrized in terms of the vector components A_0, A_1 and A_2, as in eq. (1). In the construction of these models, we implement a numerically efficient linearized approach to the lateral smoothing operator applied to the anisotropic terms. Specifically, this smoothing operator is tuned to more accurately recover the amplitude and orientation of azimuthal anisotropy in polar regions, where more traditional model-parameter-specific minimizations can introduce artefacts. The modified smoothing operator are detailed in Appendix A2.

4 TWO NEW GLOBAL MODELS OF AZIMUTHAL ANISOTROPY

We present two versions of our new model of upper mantle azimuthal anisotropy to accompany the global model SL2013sv (only the isotropic component of which was presented in Schaeffer & Lebedev 2013). The first model, SL2016svA, is the anisotropic component computed in the inversion for SL2013sv. The second model, SL2016svAr, was generated using the same data set, however using a different parametrization and less lateral smoothing; we regard this as the 'rough' version of the azimuthally anisotropic model.

The 'smooth' model, SL2016svA, is constructed on a triangular grid of knots with an average spacing of ∼280 km, and is constrained by ∼520 000 vertical component broad-band seismograms, selected (as most mutually consistent) from a total data set of almost 3/4 million. The inversion consisted of 1.55 million data equations and 1.47 million smoothing and damping constraints, to solve for 501 888 unknown model parameters. Synthetic data predicted by the final model had a variance reduction of 90 per cent with respect to those predicted by our starting 3-D reference model (with ∼6 per cent from the anisotropic terms). The lateral smoothing applied to the anisotropic terms was with coefficients almost two orders of magnitude greater than those for the isotropic model parameters (determined via examination of numerous models). We point out that SL2016svA is the anisotropic component of the inversion used to generate SL2013sv. Specifically, they are the two complements of the same inversion, where the isotropic component of SL2016svA is exactly SL2013sv.

The 'rough' model, SL2016svAr, was generated using the identical data set of ∼520 000 vertical component broad band seismogram fits as SL2016svA (and SL2013sv), but in a new inversion utilizing a different parametrization. The model grid used a greater interknot spacing of ∼390 km (the same as that used in LH2008a; Lebedev & van der Hilst 2008; Becker *et al.* 2012), but significantly less lateral smoothing, just 8× that of the isotropic velocity. The use of a slightly larger grid size and significantly smaller smoothing and damping coefficients combine to produce a model with larger amplitudes and greater lateral heterogeneity (smaller scale variations), while preserving resolving power in regions of lower sampling (i.e. the oceans). We further note that the lateral smoothing coefficients were determined subjectively through interpretation and analysis of the models. The final variance reduction for SL2016svAr is very similar to SL2016svA, slightly greater than 90 per cent (again with ∼7 per cent explained by the anisotropic terms).

The isotropic structure of the two models is very similar, as illustrated by a comparison plot in the Supporting Information (Fig. S1). There are minor variations in the strength of amplitudes (trade-offs between the A_0 and $A_{1,2}$ terms of the expansion in eq. 1), but the shape of the anomalies remains the same (trade-offs between A_0 and $A_{1,2}$ terms are discussed further below).

In Fig. 2, we plot selected horizontal cross sections through SL2016svA and SL2016svAr (see also Appendices B & C for the larger Figs B1–B3 and C1–C5, where patterns of anisotropy can be seen in greater detail). The anisotropic perturbation amplitudes are plotted as peak-to-peak values, in percent. The orientation of the fast propagation direction is indicated by the red sticks, re-sampled onto an equal area grid spaced at ∼10°.

Variations in the strength and orientation of 2Ψ azimuthal anisotropy offer a perspective on the structure and dynamics of the upper mantle, complementary to that given by the isotropic-average shear-speed variations (Schaeffer & Lebedev 2013). In our two models, the highest amplitudes of azimuthal anisotropy are located within (i) ocean basins and (ii) continental regions undergoing strong deformation.

In the smooth model SL2016svA, a clear age-dependent pattern is observed within the oceans. Beneath young oceans, the strongest amplitudes of anisotropy are observed at relatively shallow depths (50–100 km). As the oceanic lithosphere ages, the strongest anisotropy is seen at progressively greater depths. This pattern is most clear in the Pacific Ocean, where a band of largest anisotropy is shifting westward as the map-view depth increases from 110 km to 150 km and then to 200 km (Figs 2 and B2). In the rough model, this pattern is also observed, although there are also smaller regions of high amplitudes. We discuss the stratification of anisotropy beneath oceans in greater detail in Section 8.

Within continental regions, the recovered pattern of anisotropy is more complex than beneath ocean basins, with variations in orientation and amplitude occurring across shorter length scales. In SL2016svA, anisotropy amplitudes beneath continents appear to be relatively low in most places, which in part may be due to the strong lateral averaging of small- and intermediate-scale heterogeneity. Exceptions include strong anisotropy at shallower depths (≤80 km) beneath continental regions undergoing active deformation, such as the eastern Mediterranean, Tibet, and southeast Asia.

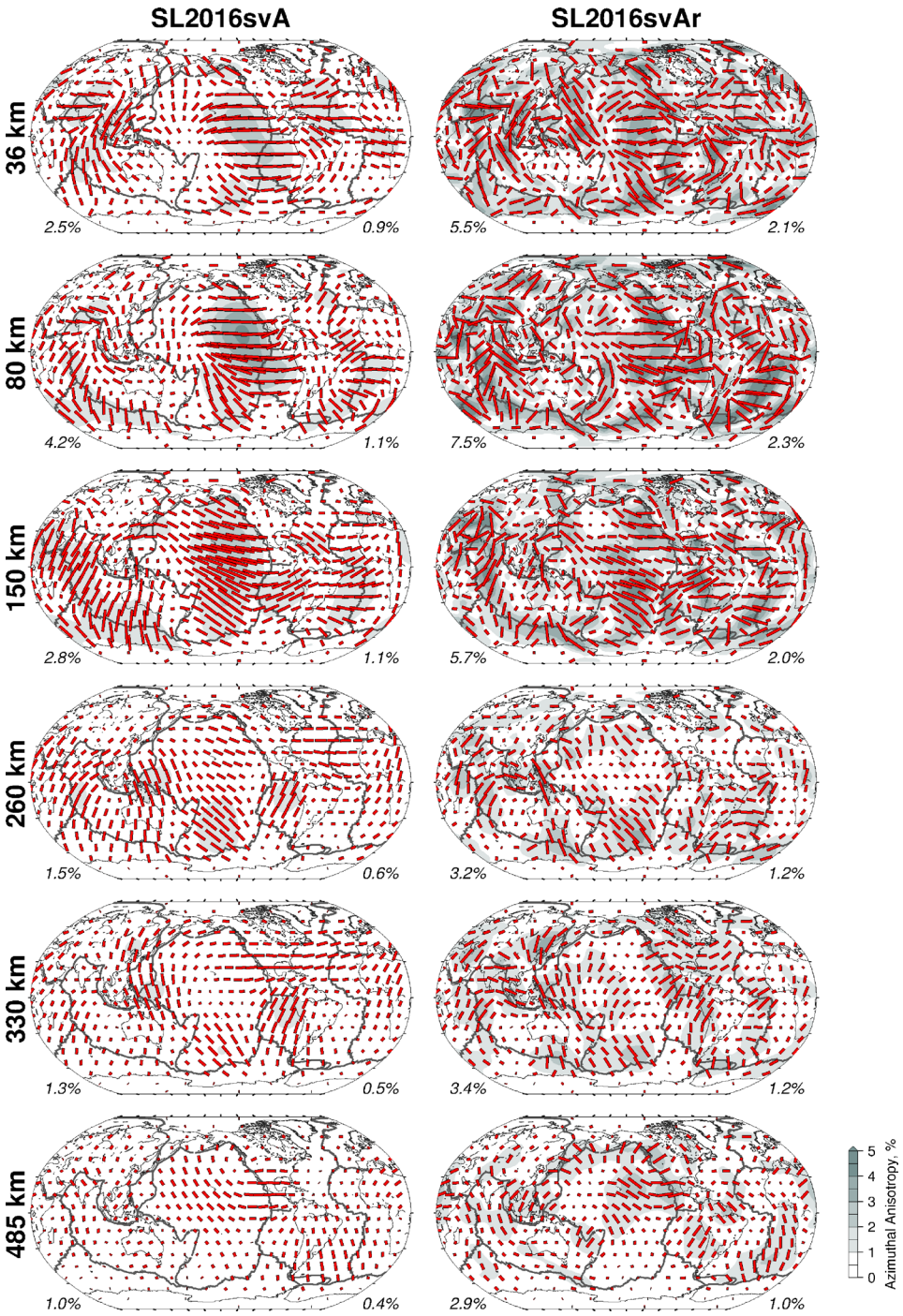

Figure 2. Slices through SL2016svA (left panels) and SL2016svAr (right panels) at six depths from the crust to the transition zone. Perturbations in peak-to-peak amplitude are indicated in per cent (from the reference), with the absolute maximum and RMS amplitude indicated at the bottom left and right of each panel, respectively. The red sticks denote the orientation of azimuthal anisotropy; their length scales with the anisotropy amplitude.

In SL2016svAr, a larger number of highly anisotropic regions is seen, including Ethiopia and the Red Sea, western (Peru, Bolivia) and southern (Chile, Argentina) South America, and eastern China. (In Section 6.4.1, we zoom in on western North America, to examine the finer scale, regional structures resolved by our global model.)

Beneath some continents (Africa, India, and Australia), the orientation of the fast-axis in the depth range of 200–350 km is roughly parallel to the absolute plate motion direction (APM; e.g. Montagner & Tanimoto 1991). In many other continental regions, however, the anisotropy mapped by global tomography is still not straightforward to explain unambiguously, and is difficult to reconcile with the results of local studies (i.e. *SKS* splitting or regional surface-wave studies).

North America is particularly well sampled in our models, resulting from the inclusion of several hundred thousand seismograms from the USArray transportable array. However, at the depth range previously interpreted to be the uppermost asthenosphere (Yuan *et al.* 2011), the orientation of anisotropy does not align with

absolute plate motion as well as that expected based on *SKS* splitting orientation (e.g. Levin *et al.* 1996; Barruol *et al.* 1997; Fouch *et al.* 2000; Currie *et al.* 2004; Eaton *et al.* 2004; Eakin *et al.* 2010; Bastow *et al.* 2011; Becker *et al.* 2012; Hongsresawat *et al.* 2015a), which at the large scale are remarkably consistent across much of North America. This alignment is also observed in models constrained jointly with *SKS* splitting measurements and other data (e.g. Marone & Romanowicz 2007; Yuan *et al.* 2011), as well as regional-scale surface wave studies (e.g. Barruol *et al.* 1997; Fouch *et al.* 2000; Deschamps *et al.* 2008a,b; Darbyshire & Lebedev 2009).

Detailed comparison between SL2016svA and SL2016svAr with other azimuthal anisotropy models and *SKS* data sets are carried out in Section 6; we first examine model resolution and trade-offs.

5 TRADE-OFFS AND RESOLUTION

We have tested the robustness of our anisotropic models in several different ways. First, we performed inversions parametrized with and without the azimuthally anisotropic terms. The comparison of the isotropic component of these models reveals that differences are small, particularly in well-sampled continental regions, with no qualitative change to their interpretation (Schaeffer & Lebedev 2013, 2015). The largest differences occur across the depth range 50–150 km in regions with sparser sampling, particularly clear within the Pacific Ocean basin. The addition of anisotropy in the inversion acts to reduce short-wavelength heterogeneity, including a northeast-southwest oriented streak of elevated velocities, similar to that observed by Ekström (2011). With the inclusion of the 2Ψ azimuthally anisotropic terms, the resulting isotropic structure across the Pacific more closely resembles the expected pattern based on the age progression of the oceanic lithosphere. In more quantitative terms, the addition of the 2Ψ anisotropy results in small changes to the isotropic structure RMS. At ∼100 km depth, the RMS difference is only 15 m s^{-1} (∼0.5 per cent of isotropic RMS); this is reduced further to only 10 m s^{-1} from 150–200 km. At greater depths, the isotropic RMS values of the models with and without anisotropy are within 3–4 m s^{-1} of each other (less than ∼0.1 per cent difference).

Second, we performed synthetic tests to quantify the leakage of isotropic structure in anisotropic and vice versa. To begin, two synthetic models are created. The first contains the isotropic structure of SL2013sv with the anisotropic terms set to zero (i.e. no anisotropy), whereas the second contains the anisotropic structure of SL2016svA with the isotropic terms set to zero (i.e. no isotropic heterogeneities). Using these synthetic models ($\underline{m}_s$), their corresponding synthetic data sets ($\underline{d}_s$) were generated through multiplication with the kernel matrix ($\underline{\underline{A}}$). The resulting synthetic data sets were inverted using the parametrization as in the generation of the original models. The results confirm the independence of the isotropic and anisotropic components, and are illustrated in Supporting Information Fig. S2. When inverting the model with no anisotropy (Supporting Information Fig. S2, right panels), the resulting maximum strength of anisotropy amplitudes are ≤0.5 per cent below 300 km and ≤1 per cent within the transition zone, with RMS values of ∼0.2 per cent and ∼0.3 per cent, respectively. When inverting the model with no isotropic structure (Supporting Information Fig. S2, left panels), the resulting maximum isotropic heterogeneities observed are ≤1 per cent below 300 km and ≤0.5 per cent in the transition zone, with RMS values of ∼0.27 per cent throughout all depths. Although the max amplitudes are somewhat larger for leakage of anisotropy into isotropic structure, this does not come as a surprise, as the isotropic structure accounts for a dominant component of the variance reduction.

Third, we have verified the sensitivity of our modelling to the vertical gradient damping coefficient (i.e. strength of vertical smoothing). The results demonstrate that the orientation of the fast directions are largely insensitive to the degree of damping. Although minor differences are observed in the strength of anisotropy, the resulting interpretations remain unchanged. We refer interested readers to the analysis for SL2016svA in the supplementary material from Becker *et al.* (2014).

Lastly, we performed a series of synthetic tests in order to query the robustness of the fast-axis orientations. This is accomplished using a 90° rotation test (Zhang *et al.* 2009; Endrun *et al.* 2011). We generate a new synthetic model by taking the anisotropy from SL2016svA and rotating the fast axis orientation by 90° (note that the isotropic structure remains unchanged). Using this synthetic model, we generate synthetic data as previously, through multiplication with the kernel matrix, and invert using regularization as in the generation of the original models. We then compare the fast-axis orientations and anisotropy amplitudes between this synthetic test and the input model (SL2016svA in this case). This test is particularly effective in detecting areas where anisotropy is affected by the isotropic heterogeneity and its sampling with the (azimuthally heterogeneous) path coverage.

The results of this comparison are shown in Fig. 3, for six depths from the crust to the transition zone. The panels on the left illustrate the angular difference between SL2016svA and the resulting model derived from the 90° rotations to SL2016svA (white means perfect recovery; red means that the anisotropy in SL2016svA in this location could be a leakage artefact). The right panels illustrate the corresponding amplitude ratios between SL2016svA and the 90° rotated version.

The angular difference in the left-hand panels gives an indication of how well the fast-direction orientation can be recovered by the data set. In regions where the angular difference approaches 0° (red), the orientation of the fast-propagation direction determined by the 90° rotated inversion recovers the same value as in the non-rotated model (SL2016svA). This suggests that the data coverage cannot resolve the orientation of anisotropy robustly. Commonly these regions overlap with areas of low-amplitudes (where any orientation can essentially be considered the same); we thus fade out regions where anisotropy amplitudes are low (≤0.25 per cent), such that these red regions are more clearly indicative of areas with limited orientation recovery. Strictly speaking, it does not preclude the orientations in these red regions from being correct, but rather that no matter what the 'true' orientation is, it will be imaged with this particular orientation. Conversely, in regions where the angular difference is ≥70° (light blue to white), the fast-axis orientations are robustly resolved and recovered given the data-coverage.

In regions where the angular difference is greater than ∼70°, the fast-axis orientations can be robustly resolved (light blue to white). In regions where the angular difference approaches 0° (red), the orientation of the fast-direction determined in the 90° rotated inversion returned to the same orientation as in the non-rotated model (SL2016svA). Normally, this is seen where the amplitude of anisotropy is low, such that any orientation is essentially the same. We thus fade out regions where anisotropy amplitudes are low, so that these red regions that remain are more clearly indicative the leakage. Strictly speaking, it does not preclude the orientations in these regions from being correct, but rather that no matter what the 'true' orientation is, it will be imaged with this particular orientation.

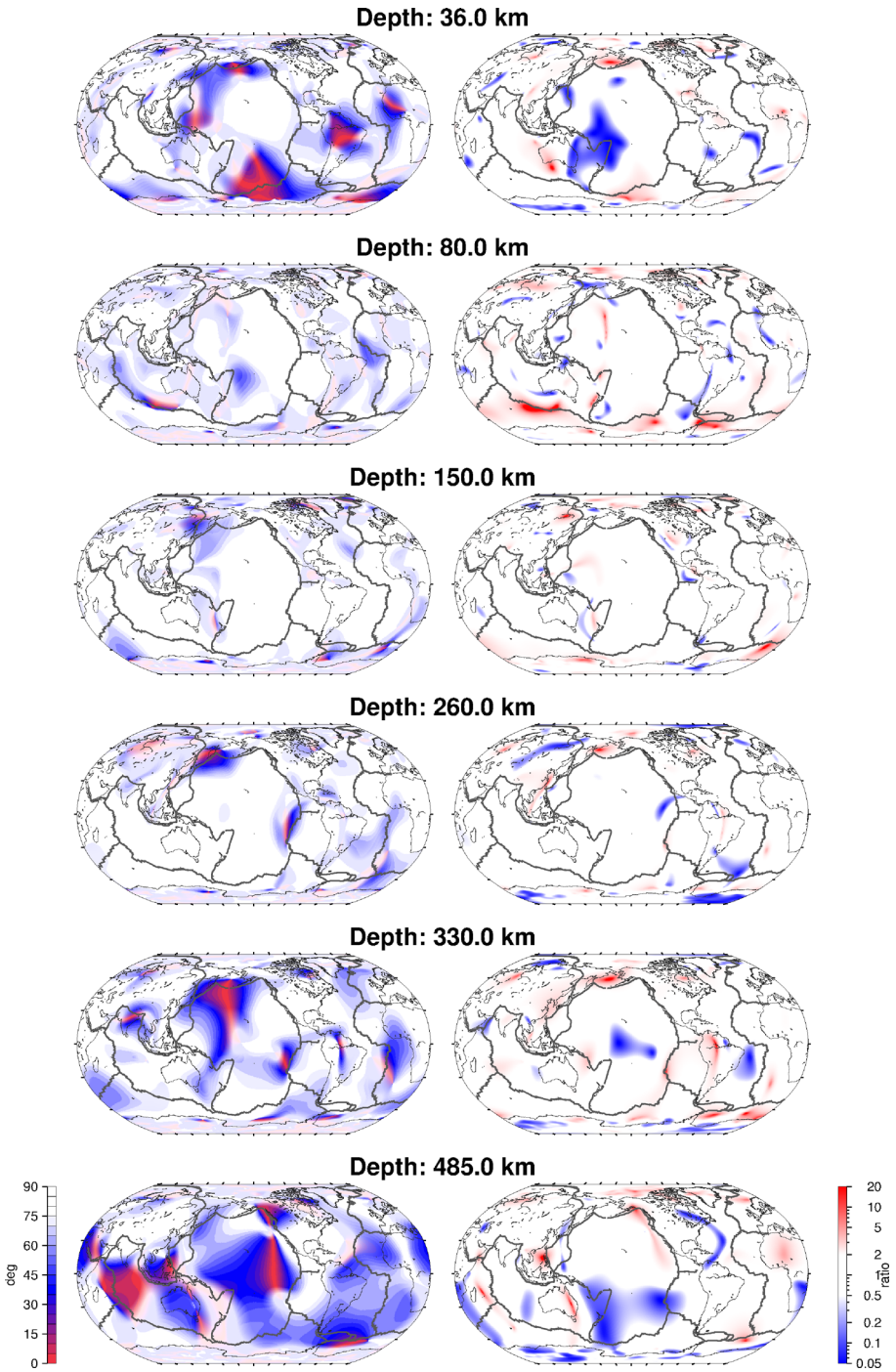

Figure 3. Anisotropy 90° rotation tests for six depths from the crust to the mantle transition zone. Left panels illustrate the angular difference between anisotropy fast directions in the actual model (SL2016svA) and in the model recovered in a resolution test using SL2016svA with anisotropy fast directions rotated by 90° as the synthetic, input model. This is effective in testing the leakage of isotropic structure into anisotropy; white and light blue regions indicate where the orientation of azimuthal anisotropy is more reliably resolved, whereas red indicates regions where the sensitivity is poorer. In regions where SL2016svA anisotropy amplitudes are small, colours have been faded towards white. The right panels illustrate a similar analysis for the recovery of amplitudes; here red indicates that amplitudes are overestimated and blue underestimated.

The amplitude ratio (Fig. 3, right) provides another indication for the robustness of anisotropy. In regions where the amplitudes between the two models strongly differ, the reliability of the model is called into question. Once again white (or light-red or light-blue) indicates better-resolved regions and bright red or blue indicate large discrepancies in the anisotropy amplitudes between the input and recovered models.

In the depth range ∼80–350 km, both anisotropy orientations and amplitudes are well resolved at the length-scales targeted by the tomography. At greater depths, such as into the transition zone, the fast-axis orientations and amplitudes are less robust. This is further borne out through comparison amongst different anisotropy models in this depth range; correlations are significantly lower in the transition zone than in the upper mantle (*cf.* Section 6.2).

6 DISCUSSION

6.1 Qualitative comparisons of global anisotropy models

Comparison of SL2016svA and SL2016svAr with other global anisotropy models can tell us what improvements in resolution the models offer. Comparisons of the current models can also show us where we are as a field: what features of upper-mantle anisotropy are resolved by many current models and where, in contrast, the models do not agree. We have compared our new models qualitatively with the global dispersion models TW2003 (Trampert & Woodhouse 2003), CLASH (Beucler & Montagner 2006) and GDM52 (Ekström 2011), and quantitatively with the global, 3-D, vertically polarized shear-velocity anisotropy models LH2008a (Lebedev & van der Hilst 2008; Becker *et al.* 2012), DR2012a (Debayle & Ricard 2013), YB13sv (Yuan & Beghein 2013) and 3D2015-07Sva (Debayle *et al.* 2016). (Note that in some cases, we append an 'a' to model names to distinguish them from their isotropic counterparts, i.e. LH2008, DR2012, 3D2015-07Sv).

LH2008a is a predecessor of our new models in the sense that it was computed with largely the same methods but with an order of magnitude less data and with greater lateral smoothing. In most regions, LH2008a is very similar to SL2016svA, except that it is smoother (Fig. 4). Within North America, however, the amplitudes in both models are small, and at 200 km depth the fast-propagation directions in SL2016svA are oriented roughly north–south, whereas in LH2008a they are more southeast-northwest. SL2016svAr shows a slightly different pattern again, but it shares more in common with SL2016svA.

One of the biggest differences between the SL2016svA models and LH2008a is the size of the data sets constraining them. In particular, a significant proportion of the coverage within North America is provided by the USArray, which LH2008a did not incorporate. A large portion of these paths sample earthquakes occurring within the highly seismogenic western Pacific. Therefore, even though the data coverage of North America is very dense, the azimuthal sampling is still highly uneven. An investigation into how we could use the dense data coverage more fully, in an optimal way, will be the subject of future work.

TW2003, CLASH and GDM52 are surface-wave dispersion models, comprising phase-velocity maps at a series of periods. In oceanic regions, the orientations of the fast axes are generally in agreement, particularly the smoothly varying ones within the Pacific Ocean basin, as well as the ones in portions of the Atlantic and Indian Oceans. Each of the models displays a decrease in anisotropy amplitude from shallow lithospheric depths (shorter to intermediate periods) through the asthenospheric mantle to the base of the upper mantle (longer periods). In SL2016svA, the maximum peak-to-peak amplitudes recovered are larger than in each of TW2003, CLASH and GDM52. For instance, in CLASH and TW2003, the maximum amplitudes between 60–100 s (corresponding to ∼60–170 km depth) are no more than 1.3 per cent (Beucler & Montagner 2006), whereas in GDM52 the maximum amplitude reaches 2.6 per cent within the period band 25–250 s (Ekström 2011). In SL2016svA and SL2016svAr, the maximum occurs at a depth of 80 km, with 4.2 per cent in the former and 7.5 per cent in the latter. (We note that in the presence of depth-dependent anisotropy the comparisons of phase-velocity and shear-velocity anisotropy amplitudes should be made with caution, as the amplitude of phase-velocity anisotropy will be reduced by the variability in the fast-propagation directions of shear-wave anisotropy with depth; we thus limit the comparison to that of the maximum amplitudes only.)

In Fig. 4, we plot three horizontal slices—at 50, 100 and 200 km—through SL2016svA, SL2016svAr, LH2008a, YB13sv, 3D2015-07Sva and DR2012a. The models DR2012a and 3D2015-07Sva are constrained by waveforms, with the inversion method built upon the secondary observables approach of Cara & Lévêque (1987). Both models used an updated implementation with improved separation of the fundamental and first five overtone measurements, compared to the older implementation (DKP2005a Debayle *et al.* 2005), as well as much larger data sets. Specifically DR2012a uses approximately 375 000 seismograms, whereas 3D2015-07Sva employs more 1.35 million. YB13sv (Yuan & Beghein 2013) utilizes the fundamental and higher mode phase velocity models of Visser *et al.* (2007) and Visser *et al.* (2008a), and inverts directly for the 2Ψ perturbations represented by the elastic parameters G_c and G_s on a $2^\circ \times 2^\circ$ global grid. The final model is limited to spherical harmonic degree $\ell = 20$, which is the harmonic degree of the input phase velocity maps. Lastly, LH2008a (Lebedev & van der Hilst 2008; Becker *et al.* 2012) was computed using essentially the same method as SL2016svA and SL2016svAr, however with a substantially smaller data set (∼50 000 successfully fit seismograms) than SL2016svA and SL2016svAr.

In terms of amplitudes, YB13sv, SL2016svAr and 3D2015-07Sva show similar maximum amplitudes and RMS perturbations. Both DR2012a and 3D2015-07Sva demonstrate locally elevated maximum amplitudes of ∼10 per cent at 50 km depth; at greater depths 3D2015-07Sva is more similar to YB13sv and SL2016svAr, whereas DR2012a maintains higher amplitudes and RMS perturbations (e.g. Yuan & Beghein 2014). We note, however, that the maxima are spatially limited to very small regions. SL2016svA has much smaller amplitudes than the previous models, but is in general higher than those of LH2008a.

The patterns of anisotropy shown by SL2016svAr, YB13sv, 3D2015-07Sva and DR2012a are also similar. SL2016svA, the smoother of our pair of models is significantly smoother than DR2012a and 3D2015-07Sva, and somewhat smoother than YB13sv. In the Pacific Ocean, the patterns of anisotropy correlate well at longer wavelengths between all three models. At shorter wavelengths, however, there are greater differences, particularly at the margins of the Pacific such as at 200 km depth beneath the Nazca plate, as well as at 110 and 200 km depth beneath the Philippine Sea Plate.

Beneath some continents (Australia, India and Africa), the anisotropy at 200 km depth is in general agreement between the different models. However, in other continental regions, the patterns are significantly different. North America is a good example: the pattern observed in DR2012a does not agree with either of the SL2016svA models, with LH2008a, YB13sv, or with APM (e.g. Montagner & Tanimoto 1991), as is discussed by Debayle & Ricard (2013).

6.2 Quantitative comparisons of global anisotropy models

In Figs 5 and 6, we present spectral correlations of six global models of azimuthal anisotropy in the upper mantle and transition zone. For each of the models the azimuthal anisotropy was expanded into generalized spherical harmonics (GSH; Phinney & Burridge 1973; Boschi & Woodhouse 2006), as described in Becker *et al.* (2007). For each pair of models, we compute the cross-correlation as a function of depth and spherical harmonic degree (centre panels). The cross-correlation as a function of depth up to degree L, r_L, is presented in each left panel for $L = \{8, 20\}$, as well as the vertically

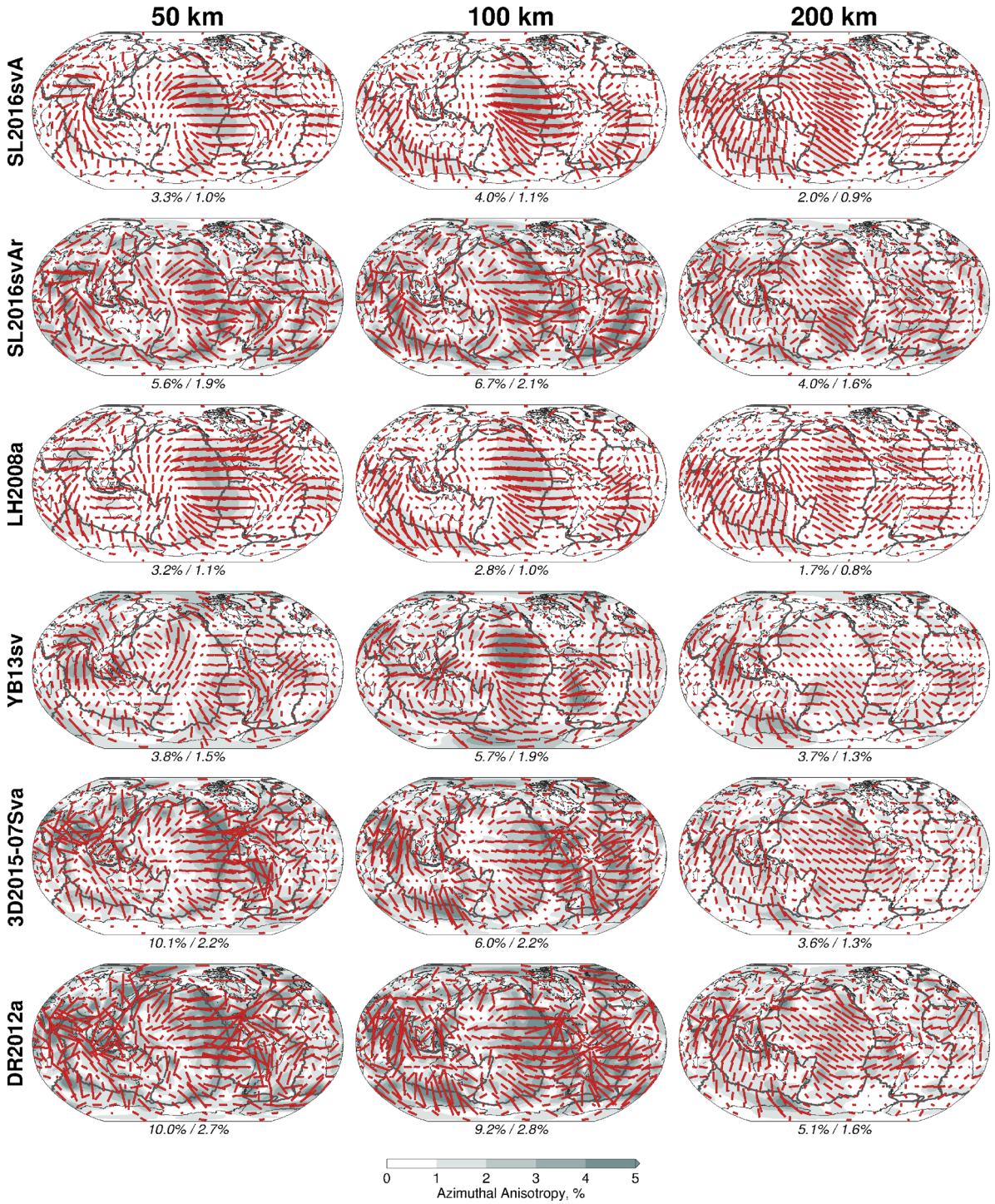

Figure 4. Horizontal slices at depths of 50, 100 and 200 km through six azimuthal anisotropy models: SL2016svA, SL2016svAr, LH2008a (Lebedev & van der Hilst 2008; Becker *et al.* 2012), YB13sv (Yuan & Beghein 2013), 3D2015-07Sva (Debayle *et al.* 2016) and DR2012a (Debayle & Ricard 2013). The same colour scale for peak-to-peak anisotropy in per cent is used in each panel (shown at the bottom). The red sticks denote the fast propagation direction as well as the anisotropy amplitude (relative lengths). The maximum amplitude and RMS amplitude of each panel are indicated beneath it.

averaged correlation, $\langle r_L \rangle$, which are indicated in the title of each panel. Lastly, the RMS amplitude as a function of depth is plotted in the right panels (note the logarithmic scale). The correlations are computed across the depth range spanning 50 to 700 km depth.

Differences in the orientation and amplitude of anisotropy in each of the models result from differences in data coverage, waveform analysis methods, treatment of errors in the measurements and how effectively their impact is minimized, and in the parametrization and regularization of the inversions. Compared to the isotropic shear-wave speed heterogeneity, anisotropic heterogeneity is weaker and, therefore more difficult to resolve. This is reflected in weaker correlations between different current anisotropy models. The largest radially averaged correlation coefficients we obtain for the large-scale, $L = 8$ heterogeneity are 0.64 for SL2016svA and LH2008a

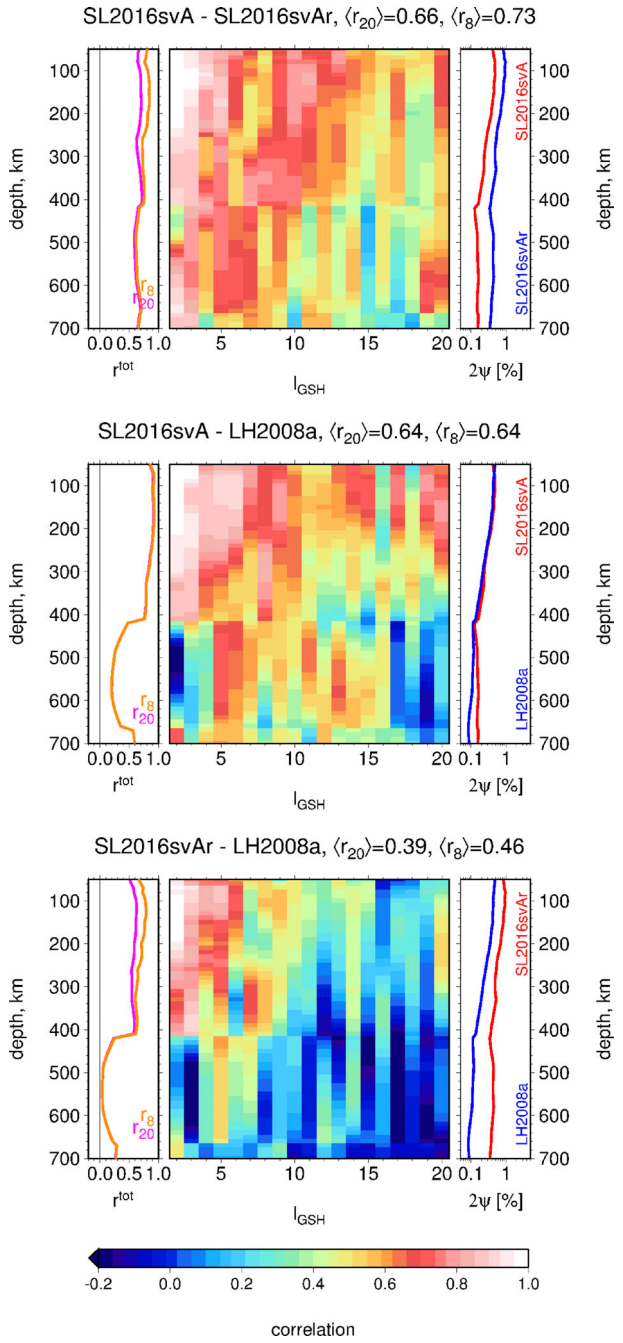

Figure 5. Spectral correlations between the two new models, SL2016svA and SL2016svAr, and LH2008a (Lebedev & van der Hilst 2008; Becker *et al.* 2012). The centre panels show the correlation coefficient as a function of spherical harmonic degree and depth, with the colour key given by the colour scale at the bottom. The right subpanels show the azimuthal anisotropy RMS amplitude, logarithmically scaled, for the two models being compared. The left subpanels indicate the average radial correlation functions for degrees up to and including 8 (orange) and 20 (purple); their radially averaged correlation coefficients are indicated in the titles of each frame.

and 0.73 for SL2016svA and SL2016svAr. This is in comparison to isotropic values, which reach average $L = \{8, 20\}$ ($\langle r_8 \rangle$, $\langle r_{20} \rangle$) correlations of $\geq$0.9 throughout the lithospheric depth range (Becker & Boschi 2002; Becker *et al.* 2007; Meschede & Romanowicz 2015).

Given that SL2016svA and SL2016svAr (and also LH2008a) are closely related, it is more telling to instead compare them with those not in the same family (e.g. DR2012a, 3D2015-07Sva and YB13sv).

The results of these comparisons are summarized in Table 1, with the $\langle r_8 \rangle$ and $\langle r_{20} \rangle$ correlations for three different depth ranges: the first covers the entire range, 50–700 km depth; second we look at just the upper mantle, 50–300 km, and finally at the base of the upper mantle and the transition zone, 300–700 km depth. In each column, the highest correlation is indicated in bold, whereas the minimum correlations are in italics. The significance of the difference between each of these correlations (following the procedure of Becker *et al.* 2007) are summarized in Tables S1 to S3 in the Supporting Information, where the upper half of each table is $\langle r_8 \rangle$ and the lower half $\langle r_{20} \rangle$.

The correlation between all models is higher in the upper mantle, 50–300 km depths, in some cases by as much as a factor of two (SL2016svA(r) with DR2012a and 3D2015-07Sva) compared with the whole depth range correlation (50–700 km). In all the depth ranges, the correlation between YB13sv with DR2012a and 3D2015-07Sva is smaller than their individual correlations with SL2016svA and SL2016svAr. This indicates that the SL2016svA(r) models contain anisotropic structures present in each of DR2012a, 3D2015-07Sva and YB13sv, but not necessarily shared between them.

The SL2016svA(r) models correlate stronger with DR2012a and 3D2015-07Sva at the shallower depths (50–300 km), and with YB13sv at greater depths (300–700 km). The correlation of DR2012a with both the SL2016svA(r) models and YB13sv in the mantle transition zone—from 410 to 660 km depth, defined by the phase transformation of olivine and to its higher pressure polymorphs—is close to zero.

Figs 5 and 6 also show the average amplitudes of anisotropy in the different models. The right-hand subpanels of each comparison show the 2Ψ RMS amplitude as a function of depth, using a logarithmic scale. At shallow depths, the RMS amplitude can vary by more than a factor of 2 between different models.

YB13sv, DR2012a, 3D2015-07Sva and SL2016svAr show a relatively higher RMS amplitudes down to the base of the transition zone (Yuan & Beghein 2014), compared to SL2016svA and LH2008a. This is to be expected as the latter models are by design smoother with overall lower amplitudes. The radial correlations r_8 and r_{20} show also significant decreases with depth.

The average angular misfits between the fast-direction azimuths in different models provide a quantitative assessment of the similarities in the orientations. The depth dependence of the average angular misfits offer another indication of the depth ranges across which the orientations of azimuthal seismic anisotropy can be considered robustly resolved by the current generation of models. At the depths where the average seismic anisotropy orientations are similar between different models (i.e. the average misfits are low), the recovered anisotropy can be considered more reliable.

In Fig. 7, we summarize the angular misfit of DR2012a, 3D2015-07Sva, YB13sv, LH2008a and SL2016svAr with respect to SL2016svA as a function of depth. At each depth, the averages are computed globally (solid curves), beneath oceans (dashed curves), and beneath continental regions (dotted curves) from maps of misfit, such as those presented in Supporting Information Fig. S3 for depths 50, 100 and 200 km. An average angular misfit of 45° would indicate a random orientation between the models, whereas a value of $\langle \Delta\alpha \rangle = 20°$ represents a strong match between the models (e.g. Becker *et al.* 2014).

Clearly the closest match with SL2016svA is LH2008a with a depth-averaged global misfit of ~11°, followed by the rough version SL2016svAr with an average misfit of ~18°. In both cases, their profiles are almost vertical, indicating that the average

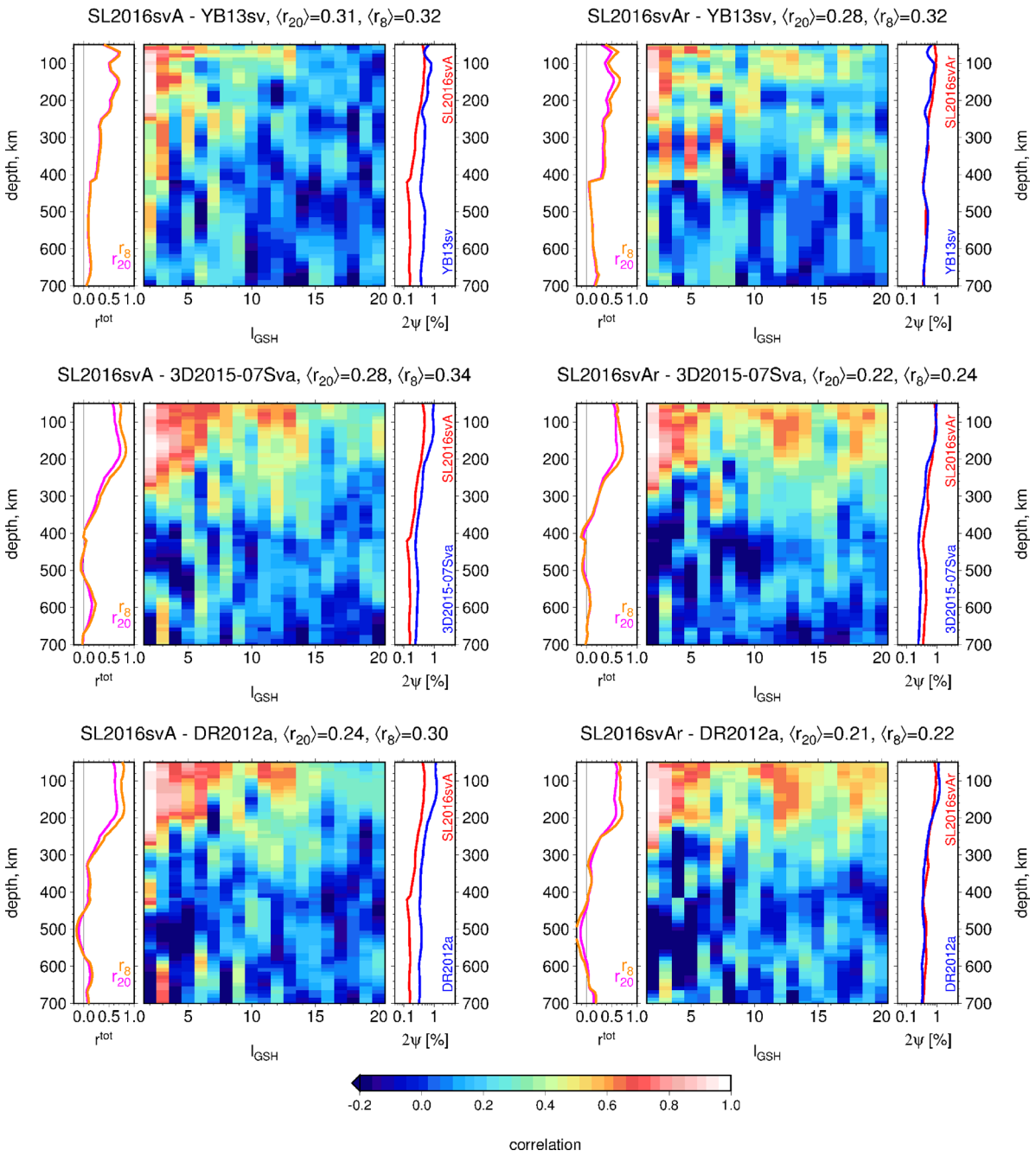

Figure 6. Spectral comparisons of SL2016svA and SL2016svAr with three other global seismic anisotropy models: YB13sv (Yuan & Beghein 2013), 3D2015-07Sva (Debayle *et al.* 2016) and DR2012a (Debayle & Ricard 2013). Plotting conventions follow those of Fig. 5.

Table 1. Radially averaged correlation coefficients $\langle r_L \rangle$, for degrees up to $L = 8$, 20. Three different depth ranges are summarized: 50–700, 50–300 and 300–700 km. In each column, the maximum correlation is indicated in bold, whereas the minimum is in italics.

	50–700 km		50–300 km		300–700 km	
Models	$\langle r_8 \rangle$	$\langle r_{20} \rangle$	$\langle r_8 \rangle$	$\langle r_{20} \rangle$	$\langle r_8 \rangle$	$\langle r_{20} \rangle$
SL2016svA - YB13sv	0.32	**0.31**	0.53	0.51	0.17	0.16
SL2016svAr - YB13sv	0.32	0.28	0.49	0.41	**0.20**	**0.18**
SL2016svA - DR2012a	0.30	0.24	0.65	**0.52**	0.05	0.04
SL2016svAr - DR2012a	0.22	0.21	0.54	0.47	*−0.01*	*0.02*
SL2016SvA - 3D2015-07Sva	**0.34**	0.28	**0.68**	0.57	0.10	0.08
SL2016SvAr - 3D2015-07Sva	0.24	0.22	0.56	0.50	0.02	0.03
YB13sv - DR2012a	*0.16*	*0.15*	*0.36*	*0.30*	0.02	0.03
YB13sv - 3D2015-07Sva	0.18	0.17	0.36	0.31	0.06	0.06

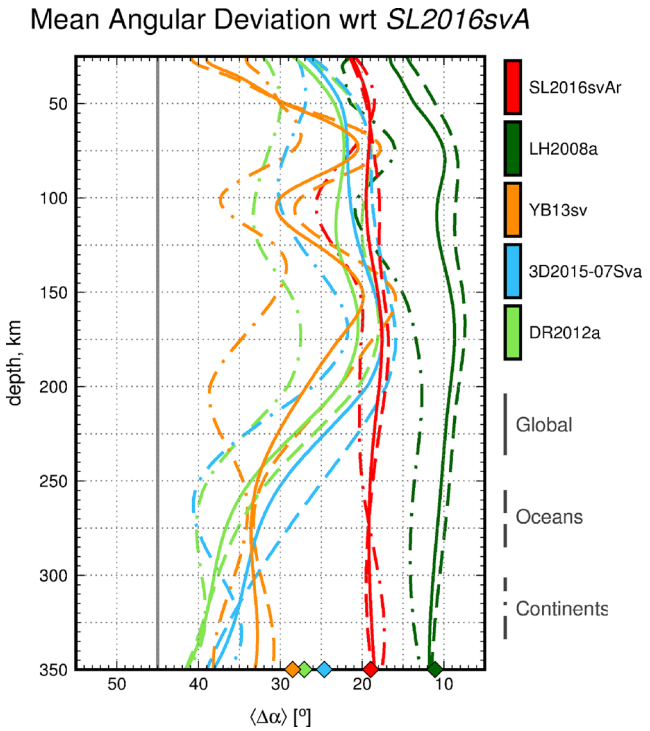

Figure 7. Average angular deviation $\langle \Delta\alpha \rangle$ with respect to the orientations of SL2016svA as a function of depth, for DR2012a (light green; Debayle & Ricard 2013), 3D2015-07Sva (light blue; Debayle *et al.* 2016), YB13sv (orange; Yuan & Beghein 2013), LH2008a (dark green; Lebedev & van der Hilst 2008; Becker *et al.* 2012), SL2016svAr (red). Solid curves denote the global averages, dashed curves for oceanic regions only, and dash-dotted curves for continental regions. Filled diamonds along the bottom axis indicate the depth-averaged global misfit for each model. Light grey line at $\langle \Delta\alpha \rangle = 45^\circ$ indicates a random average orientation between a pair of models.

angular misfit is almost insensitive to depth. This is contrary to angular misfit with the other three models, which show a strong depth dependence. Global angular misfits for DR2012a, 3D2015-07Sva and YB13sv attain their minimum values (best match), compared with SL2016svA, at depths shallower than 200 km. The greater misfits at greater depths is likely due to differences in effective data coverage afforded by the different ways of including structural information resolved by higher modes, as well as inversion parametrizations.

6.3 Global comparisons with *SKS* splitting

In this section we compare our new models of azimuthal anisotropy (SL2016svA and SL2016svAr) and the four other models (LH2008a, YB13sv, DR2012a and 3D2015-07Sva) with a global compilation of SKS-splitting measurements. The models have been expanded up to angular degree 20 ($L = 20$) using generalized spherical harmonics in order to perform quantitative comparisons, following the procedure of Becker *et al.* (2012). The degree-20 global representation of *SKS* splitting (in the figures labelled as *SKS*) was derived by Becker *et al.* (2012) from more than 5000 station-averaged measurements, based on the compilations of Silver (1996), Fouch (2003), Wustefeld *et al.* (2009) and additional studies. We note that there are few oceanic *SKS* observations, therefore the oceanic regions in the GSH *SKS* expansion are more poorly constrained than continental areas.

In Fig. 8, fast directions of the 2Ψ azimuthal anisotropy of SL2016svA (top) and SL2016svAr (bottom) are plotted as green sticks on top of those of the global SKS-splitting distribution (magenta sticks). The background colours indicate the angular misfit, $\langle \Delta\alpha \rangle$. (The equivalent angular misfits for LH2008a, DR2012a, 3D2015-07Sva and YB13sv are plotted in Supporting Information Fig. S5).

At 125 km depth (left), the angular misfit between seismic anisotropy fast directions given by tomography and *SKS* splitting is consistently lowest (best match) beneath ocean basins, compared to continental regions, for all models (Fig. 8 and Supporting Information Fig. S5). This is in part due to the generally smoother, longer-wavelength structural heterogeneity across the ocean basins, compared to the shorter-wavelength heterogeneity within continents, and in part due to the continental lithosphere often being thicker, with layering of anisotropy within it. At 250 km depth, in contrast, the angular misfit between the data sets is typically lower beneath the continents than beneath the oceans, as clearly seen in the depth-averaged angular misfits (derived from maps such as those in Fig. 8 and Supporting Information Fig. S5), plotted in Fig. 9. The oceanic average is indicated by solid lines, the continental by dashed lines, and the global depth-averaged misfit as diamonds on the lower axis.

The angular misfit is lower within oceanic regions at depths shallower than ∼175–225 km, and below these depths continental regions show a lower misfit for all models except DR2012a. The oceanic misfits are particularly low for the smoothest SL2016svA and LH2008a models. The transition depth—the depth where the oceanic and continental misfit curves cross over—is 200 ± 20 km for SL2016svA, SL2016svAr, LH2008a and YB13sv.

Although *SKS* splitting measurements average over the entire crust-mantle column, the dominant contribution to the splitting is typically considered to arise from the upper mantle (lithosphere and asthenosphere), with deeper upper mantle anisotropy (≥200 km) demonstrated to play a significant role (Yuan & Beghein 2013). Assuming that most of the *SKS* splitting accumulates largely from the asthenosphere, the observed cross-over in the depth-dependent misfit between anisotropy from tomography and from *SKS* splitting measurements is due to the thicker lithosphere beneath stable continents (*cf.* Yuan *et al.* 2011).

Fig. 10 shows the correlation of the six tomographic anisotropy models and the *SKS* expansion as a function of depth (20–400 km) and angular degree ($\ell\{2, 20\}$). For all models, the highest correlations occur at $\ell \leq 5$, and dominantly in the depth range between 50 and 250 km. These lowest degree patterns account for the large-scale anisotropic domains beneath oceans and probably, also, the ocean-continent dichotomy, with smoothly varying patterns in the oceans and more spatially variable patterns in continental regions. In SL2016svA, SL2016svAr and LH2008a, increased correlation is observed across almost the entire depth range for $\ell = 9$; this suggests that there exists some patterns at long to intermediate wavelengths (∼4000–2000 km) which are well correlated within the upper mantle. These same bands of increased correlation spanning the entire depth range are not as obvious in DR2012a and 3D2015-07Sva, which show a lesser degree of vertical coherence within any particular angular degree. We note however, that this is by design, as these models were specifically constructed with little vertical smoothing (Debayle & Ricard 2012). We further note a strong correlation throughout most of the upper mantle at $\ell = 3$ for SL2016svA, SL2016svAr, LH2008a and YB13sv; similarly for DR2012a and 3D2015-07Sva a band at $\ell = 4$ is observed through the lower 2/3 of the upper mantle. These correspond to very long wavelength patterns (≥13 000 km), much larger than those

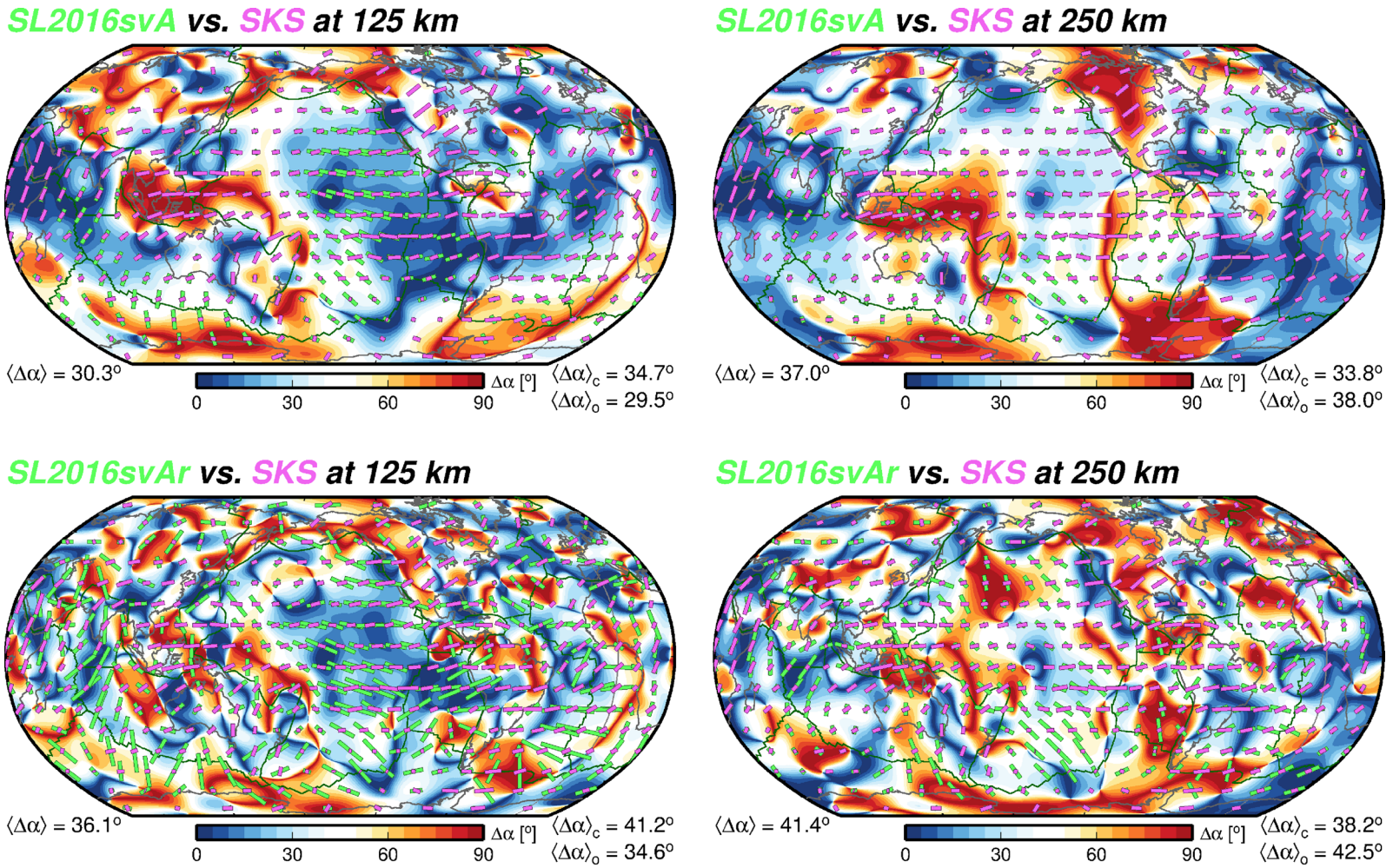

Figure 8. Comparison of the fast propagation directions according to the models SL2016svA and SL2016svAr (cyan sticks) and to the global *SKS* splitting distribution (green sticks) from Becker *et al.* (2012), for depths of 125 and 250 km. For both the tomographic models and *SKS* splitting, anisotropy was expanded in generalized spherical harmonics up to the maximum angular degree 20. The colour scale indicates misfit in azimuthal anisotropy orientation between the models, with weighting based on the amplitude of the tomography model.

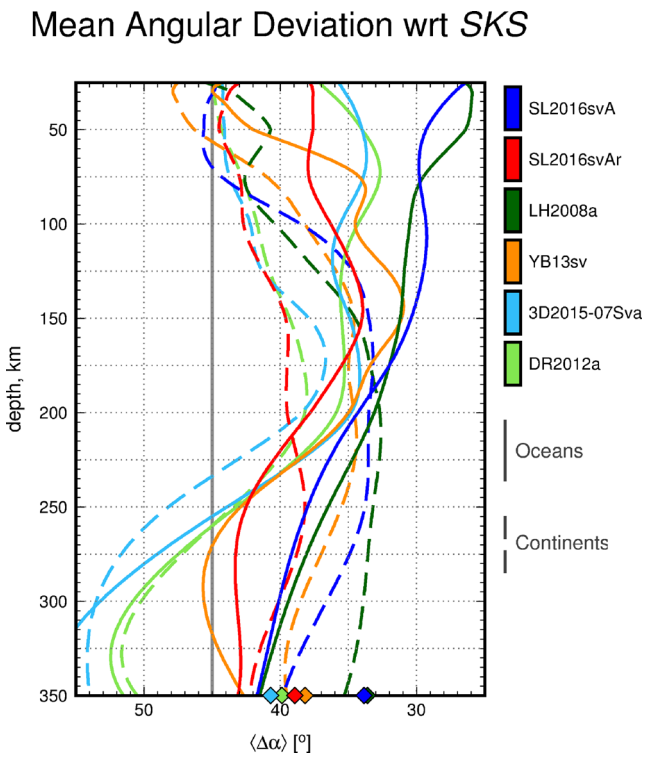

Figure 9. Average angular deviation $\langle \Delta\alpha \rangle$ with respect to the global *SKS* splitting expansion of Becker *et al.* (2012) as a function of depth, for SL2016svA (black), SL2016svAr (red), LH2008a (dark green; Lebedev & van der Hilst 2008; Becker *et al.* 2012), YB13sv (orange; Yuan & Beghein 2013), 3D2015-07Sva (light blue; Debayle *et al.* 2016), and DR2012a (light green; Debayle & Ricard 2013). Solid curves denote the average across oceanic regions, dashed curves for continental regions. Filled diamonds along the bottom axis indicate the depth-averaged global misfit for each model. Light grey line at $\langle \Delta\alpha \rangle = 45^\circ$ indicates a random average orientation between the two models.

expected within continents. This strong correlation may potentially result from the reduced sampling of the oceanic regions compared to the continents, where interpolation in the generation of the *SKS* expansion and smoothing in the tomographic models results in an apparent strong correlation.

Of the five models, LH2008a has the highest overall depth-averaged $\langle r_8 \rangle$ and $\langle r_{20} \rangle$ correlation coefficients with the *SKS* distribution, 0.26 and 0.24, respectively. The smoother of our two new models, SL2016svA, is a close match with $\langle r_8 \rangle = 0.22$ and $\langle r_{20} \rangle = 0.21$. The rougher model SL2016svAr has yet lower overall correlation values of $\langle r_8 \rangle = 0.14$ and $\langle r_{20} \rangle = 0.12$. YB13sv has a slightly larger correlation than SL2016svAr (*cf.* Becker *et al.* 2012). The total correlation values for DR2012a and 3D2015-07Sva are very close to zero through the upper mantle. However, we also observe a negative correlation coefficient at depths greater than ∼250 km depth, which would contribute to reducing the depth-averaged total correlation.

It is clear that the similarity between the different current tomographic models of azimuthal anisotropy is significantly greater than their similarity with the expanded *SKS* data set (*cf.* Becker *et al.* 2012). Despite the expansion of the *SKS* measurements to the same spherical harmonic degree, the relatively poorer correlation with *SKS* likely reflects both the spatial sampling of the measurements and their inherent length-scale of heterogeneity. Specifically, *SKS* measurements are available predominantly within the continents, where fast-directions are likely to vary over spatial length scales that cannot yet be fully resolved by global surface wave tomography models. In the oceans, where the patterns are expected to vary more smoothly and hence be better resolved by tomography models, there are substantially fewer *SKS* measurements upon which the expansion is based. We emphasize, however, that even though the tomography-SKS correlation is lower than intertomography model correlations, Becker *et al.* (2012) demonstrate that the correlations between tomography models and *SKS* splitting are statistically significant.

6.4 Regional examples

The rougher version of our model, SL2016svAr, targets higher resolution and resolves regional-scale patterns of anisotropy beneath well-sampled areas, in particular densely instrumented regions on continents. Western North America and Tibet and East Asia are two examples of how the global anisotropic tomography reveals the layering of anisotropy and deformation at regional scales.

6.4.1 Deformation within western North America

With the deployment of the USArray across the United States, beginning in the west, there have been many studies carried out on the western, deforming margin of the North American continent, using a variety of seismic techniques. We incorporate the USArray data into our data set, and the resulting models should resolve the finer scale features. As we have already discussed, however, North America is enigmatic, in that the anisotropy derived solely from surface wave tomography and that from *SKS* measurements often do not match.

The stratification of azimuthal anisotropy beneath North America has recently been studied by joining surface-wave and *SKS*-splitting data (Yuan *et al.* 2011). At the continental scale, a contrast in the orientation of anisotropy between the actively deforming western United States and the stable eastern-central part of the continent was observed to coincide with the Cordilleran deformation front (*cf.* Hongsresawat *et al.* 2015b). The anisotropy imaged by Yuan *et al.* (2011) beneath the actively deforming western margin, presented at depths 70 km and deeper, is oriented approximately southwest–northeast at 70 km and gradually rotates to a more east–west orientation by 150 km depth. At 200 km, fast directions are oriented northwest–southeast, roughly aligned with the Pacific Plate APM (HS3-Nuvel 1A Gripp & Gordon 2002).

In Fig. 11, SL2016svAr is plotted within the western US at three depths between 56 km and 200 km. The isotropic perturbations in the background are as in SL2013sv, with the scale saturated at ±8 per cent. The grey sticks show the orientation and magnitude of anisotropy, and are scaled consistently at all depths. The maximum anisotropy we detect in this region (at these depths) is ∼4.8 per cent.

At the shallowest depth of 56 km, the orientation of the fast axis of anisotropy inland is similar to that mapped at intermediate periods by Lin *et al.* (2010), who used a combination of ambient noise and earthquake data recorded at stations of the USArray. Unlike the array-based results, our model also shows anisotropy outside the footprint of the array. We observe a sharp change in the orientation of the anisotropy at the continent's boundary with the Pacific Ocean, where the anisotropy aligns with APM.

At greater depths (110 km), the pattern of anisotropy is similar to that mapped by Yuan *et al.* (2011). At shallower, lithospheric depths, however, the transition in orientation stepping into the Pacific Ocean basin is sharper in SL2016svAr. At all depths shallower than 110 km,

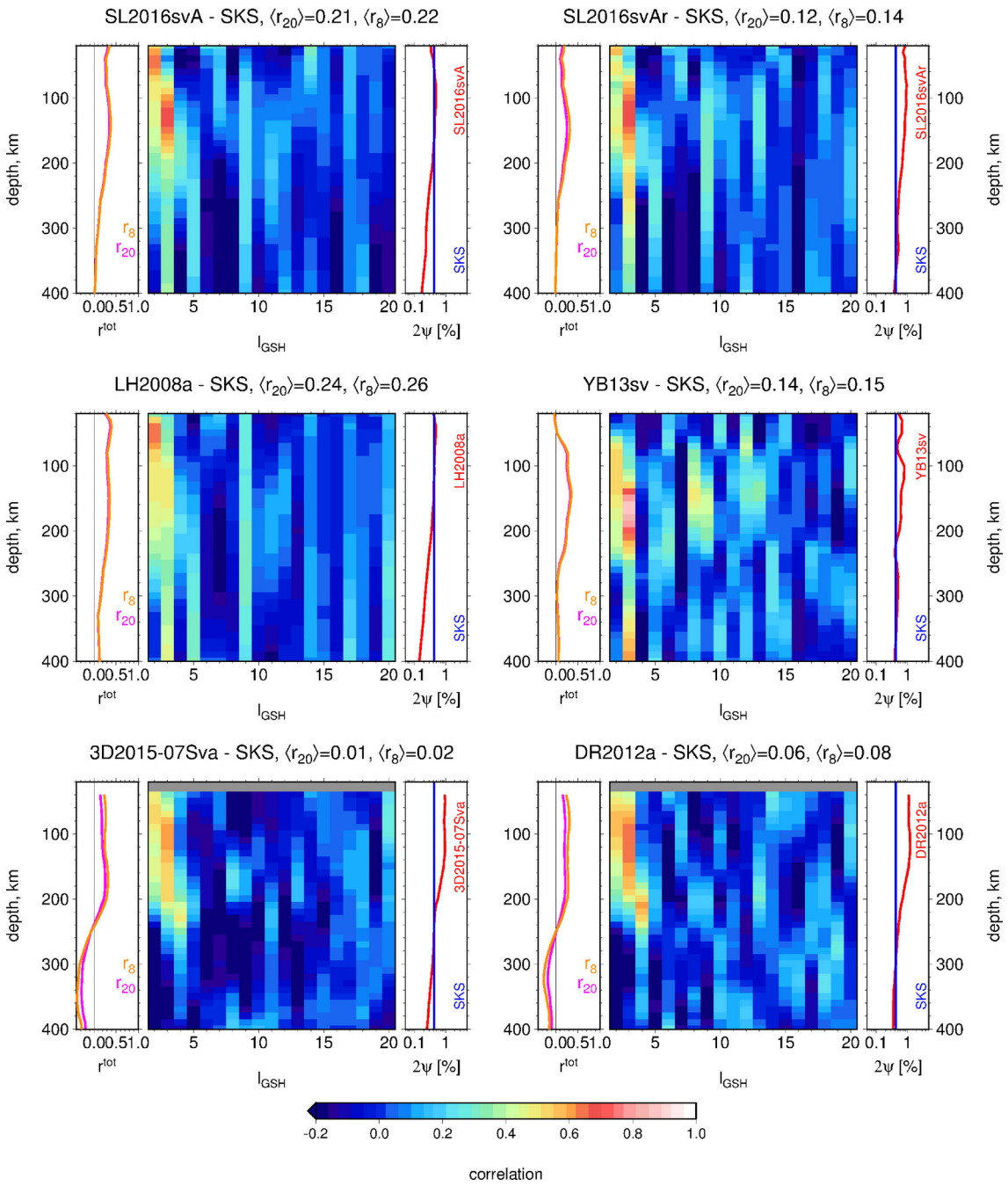

Figure 10. Correlations of six global tomographic models of 2Ψ anisotropy—SL2016svA, SL2016svAr, LH2008a (Lebedev & van der Hilst 2008; Becker *et al.* 2012), YB13sv (Yuan & Beghein 2013), 3D2015-07Sva (Debayle *et al.* 2016) and DR2012a (Debayle & Ricard 2013)—with a degree-20 generalized spherical harmonic expansion of the global *SKS* splitting database (Becker *et al.* 2012). The central subpanels: depth-degree correlation coefficients; left: correlations as a function of depth for the expansions up to degrees 8 (orange) and 20 (pink); right: RMS amplitudes. Each tomographic model was expanded up to degree 20 for the comparison. Note that the maximum depth here is 400 km, instead of 700 km as in Fig. 5.

the orientation is observed to change very sharply coincident with the Cordilleran deformation front (dashed-green line).

At 200 km, the pattern of anisotropy is no longer similar to the results of Yuan *et al.* (2011). The NNW–SSW orientation beneath the continent does not match either the Pacific or North American APM. The western US Cascades separate the domain with the NNW–SSW fast directions within the continent (which could be considered trench-parallel, next to the location of the current and recent subduction) from the domain with APM-parallel fast directions beneath the Pacific Plate.

6.4.2 Azimuthal anisotropy beneath southeastern Eurasia

In Fig. 12, we plot the anisotropic structure resolved beneath southeastern Asia and India, with a focus on the pattern of anisotropy associated with the convergence of India and Eurasia. The strength of anisotropy is indicated by the background colour (peak-to-peak amplitudes), whereas the red sticks denote the orientation and amplitude of anisotropy in SL2016svAr.

At 56 km, a strong anisotropy anomaly underlies the Tibetan Plateau and surroundings. The partially molten Tibetan middle crust

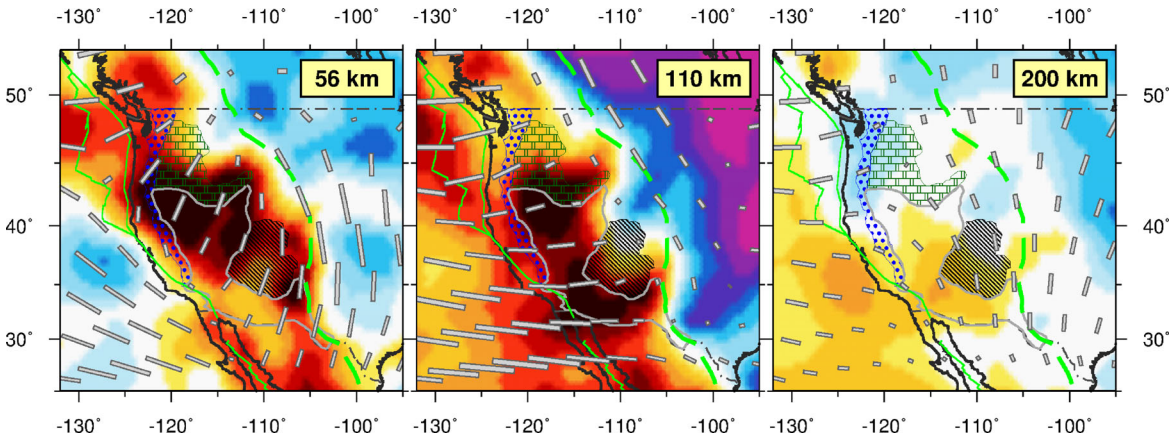

Figure 11. Azimuthal anisotropy beneath the western United States, as imaged by SL2016svAr. Isotropic perturbations are with respect to our 1-D mantle reference model (Schaeffer & Lebedev 2013) and saturate at 8 per cent for all depths. The anisotropy is plotted on the model grid (390 km knot spacing), with the length of the sticks indicating the strength of anisotropy. The largest amplitude is approximately 4.8 per cent, and the scale is consistent at all depths. The solid green lines indicate the plate boundaries; the dashed green line denotes the Cordilleran deformation front. The blue hashed region represents the western US Cascades, the dark green hashing the Snake River Plains, the black hashed region the Colorado Plateau, and the light-grey outlined region the Basin and Range.

is thought to be sheared strongly by an eastward flow towards and around the Eastern Himalayan Syntaxis (e.g. Nelson *et al.* 1996; Agius & Lebedev 2014). The anisotropy observed at these shallow depths in SL2016svAr corroborates this view. The anisotropy within the central plateau is oriented east-west. Around the Eastern Syntaxis, the fast-propagation directions rotate into a southwest-northeast orientation at 36 km (not shown) and slightly more north-south at 56 km. At a depth of 80 km (Fig. C1), anisotropy no longer rotates at the eastern syntaxis in its orientation.

The orientation at 36 km, 56 km, and 80 km depths (Figs 12 and C1) are also in good agreement with the results from recent regional anisotropy studies carried out using stations across the plateau (e.g. Yang *et al.* 2010; Agius 2012; Pandey *et al.* 2015). Both the orientations and amplitudes of anisotropy are consistent between SL2016svAr and the regional phase-velocity tomography and V_s anisotropy profiles.

At 110 km depth (Fig. 12) beneath India and the Arabian Sea, re-orientation of the fast axis of propagation from an approximately E-W orientation to SSW-NNE is observed. The subplate, asthenospheric anisotropy aligns with the rapid northward motion of India in the late Cretaceous, followed by its slower but continuing movement towards the NNE over the last 50 million years. Beneath the Himalayas, anisotropy is oriented along the strike of the suture from 36 km down to approximately 150 km. By 200 km depth, the anisotropy is distributed in a more continuous southwest-northeast pattern, extending from India into Asia.

7 IMPLICATIONS FOR THE PRESENCE OF ANISOTROPY IN THE DEEP UPPER MANTLE AND TRANSITION ZONE

The presence of intrinsic anisotropy in the deep upper mantle and transition zone has been a subject of debate over the previous several decades. Its seismic detection is difficult, and large discrepancies remain amongst different studies that report it (Montagner & Kennett 1996; Trampert & van Heijst 2002; Beghein & Trampert 2004; Panning & Romanowicz 2006; Visser *et al.* 2008b).

In the upper mantle shallower than ∼250 km depth, the LPO of olivine is typically invoked to explain seismic observations, as it is the most volumetrically abundant mineral and as it has large single-crystal anisotropy (Mainprice *et al.* 2005). At subasthenospheric depths below ∼200–250 km, it was proposed that the rapid decrease in anisotropy at the Lehmann discontinuity marked the transition from the dislocation to diffusion creep regime (Karato 1992; Gaherty & Jordan 1995). A similar depth was utilized by Dziewonski & Anderson (1981) in the construction of the Preliminary Reference Earth Model (PREM), which is isotropic at depths greater than the 220 km, the Lehmann discontinuity. Recent results have demonstrated that dislocation creep may still dominate at depths to the base of the upper mantle, though perhaps with a different type of fabric (Mainprice *et al.* 2005; Becker *et al.* 2008). Independently, regional and global seismic studies demonstrated the presence of anisotropy below 220 km (e.g. Trampert & van Heijst 2002; Visser *et al.* 2008a; Lebedev *et al.* 2009), as well as in the transition zone (e.g. Yuan & Beghein 2013, 2014).

Previous generations of global azimuthal seismic anisotropy models (e.g. TW2003, DKP2005a, LH2008a) showed low amplitudes within the deep upper mantle and transition zone. Some of the more recent models (e.g. YB13sv, DR2012a, 3D2015-07Sva and SL2016svAr) show relatively higher RMS amplitudes of anisotropy at depths greater than ∼300 km; these were summarized in Figs 5 and 6, in the right-hand subpanels. However, intermodel correlation as a function of depth between the models with high RMS amplitudes in the transition zone is close to zero at the transition zone depths (left-hand subpanels, Fig. 6).

To more clearly demonstrate the strong contrast in model correlation between the upper mantle and lower parts of the upper mantle and transition zone, in Fig. 13 we plot the total model correlation values for two different depth ranges: 50–300 km (left panel) and 300–700 km (right panel). Each square in the two panels illustrates the radially averaged degree 8 correlation $\langle r_8 \rangle$ (*cf.* Becker *et al.* 2007). The models are labelled along the left and bottom axes, with their average correlation (excluding their auto-correlation) labelled along the right axis. This total correlation is used to sort the models, with the highest correlations at the bottom-left and lowest at the top-right.

The warmer colours in the left panel, compared to the cooler colours in the right panel, clearly indicate that shallower depths are more robustly resolved amongst the different models. The low correlation values below ∼250–300 km depths suggest that the

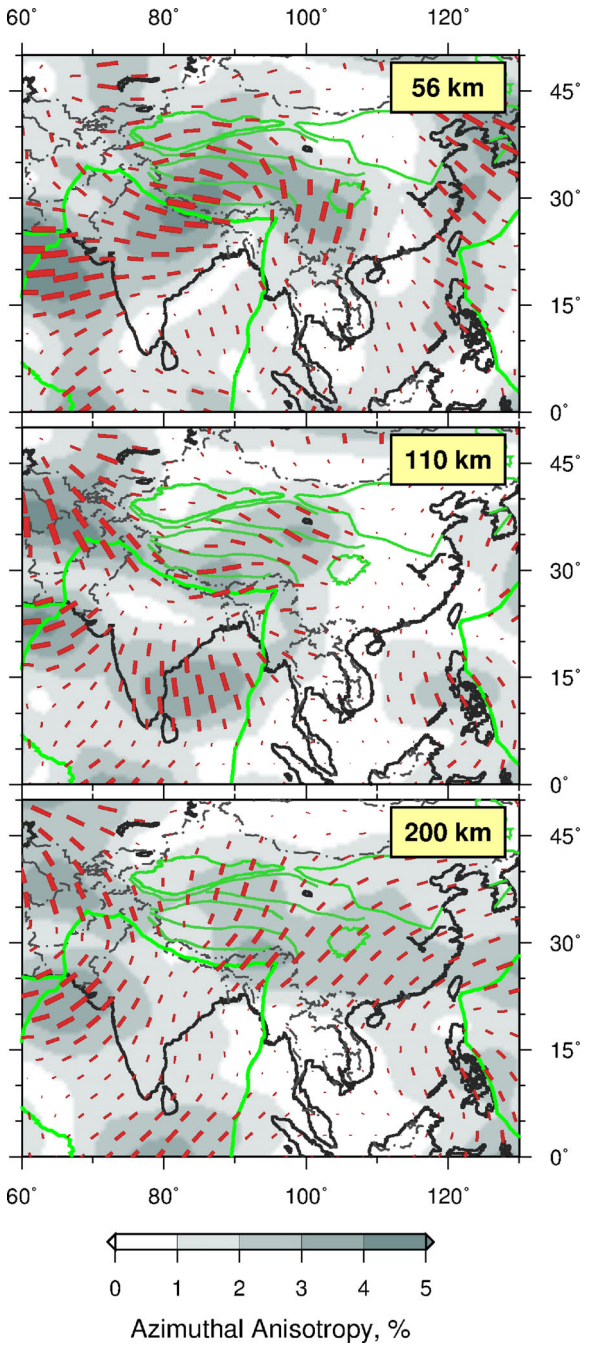

Figure 12. Distribution of azimuthal anisotropy in and around the India-Asia collision zone, as imaged by SL2016svAr. The anisotropy is plotted on the model grid (390 km knot spacing), with the length of the stick indicating the strength of anisotropy. The largest amplitude is approximately 5.8 per cent, and the scale is the same at each depth. The relative amplitudes of anisotropy (percent) are with respect to our 3-D crustal reference model at 56 km (within the thick crust beneath Tibet) and with respect to our mantle reference elsewhere. Grey lines denote the main tectonic boundaries in the region.

anisotropic structures in the models have little similarity even at the very longest wavelengths. If we exclude the correlations between models of the same family (SL2016svA, SL2016svAr, LH2008a), then the highest average correlation across the depth range 300–700 km is just 0.2, between SL2016svAr and YB13sv. The equivalent 50–300 km correlation is more than a factor of two higher.

For completeness, we include similar analysis for slightly modified depth ranges in Fig. S6, using 50–200 and 200–700 km. As is expected based on Fig. 7, the correlations for 50–200 are higher than for 50–300 km. Similarly, the equivalent 200–700 km correlations are higher than the 300–700 km, as although still small, the model correlations between 200–300 km is still larger than those within the transition zone, therefore elevating the total depth-averaged correlation.

In recent studies, Yuan & Beghein (2013) and Yuan & Beghein (2014) generate quantitative estimates of the strength and orientation of azimuthal anisotropy in the deep upper mantle and transition zone. Their results indicate that anisotropy is required through the upper mantle, and, that average anisotropy changes at the transition zone discontinuities. Given the low correlation between current global azimuthal seismic anisotropy models below ∼300 km depth, however, we would suggest caution in the interpretation of patterns of seismic anisotropy at this greater depth range. The comparison of SL2016svA with SL2016svAr typifies the challenge associated in accurately recovering the anisotropic amplitudes. Although these models are constructed using the same data set, the choice of regularization during the inversion has a significant effect on the recovered amplitude (see Fig. 5). This effect of the inversion parameters, with little impact on the model misfit and remaining variance, suggests that the data does not have a strong sensitivity in this depth range.

8 THE THICKNESS OF TECTONIC PLATES

The pattern of seismic anisotropy fast propagation directions within ocean basins have been subject of inquiry for the last half century. At the most basic level, two patterns of anisotropy are observed (Hess 1964; Forsyth 1975; Nishimura & Forsyth 1989; Montagner & Tanimoto 1991; Smith *et al.* 2004; Maggi *et al.* 2006; Debayle & Ricard 2013; Becker *et al.* 2014; Burgos *et al.* 2014), with their differences providing key insights into the vertical stratification of deformation across the boundary layer separating the rigid lithosphere from the low-viscosity asthenosphere beneath it.

At shallower depths—within the mantle lithosphere—the alignment of seismic anisotropy matches well with the alignment of intrinsically anisotropic olivine crystals expected from ‘frozen-in’ fabrics, generated at the time of the plate formation (Smith *et al.* 2004; Maggi *et al.* 2006; Debayle & Ricard 2013). These ‘palaeospreading’ orientations can be computed readily from the gradient of sea floor ages (e.g. Conrad & Lithgow-Bertelloni 2007).

At greater depths, a coherent alignment of seismic anisotropy with current, or geologically recent plate motions is observed (Tanimoto & Anderson 1984; Nishimura & Forsyth 1989; Montagner & Tanimoto 1991; Smith *et al.* 2004; Maggi *et al.* 2006; Becker *et al.* 2014). Assuming, as a first-order approximation, that the mantle beneath moving plates is stationary, the plate motions—and hence surface velocities—can be directly related to the development of fabrics within the asthenosphere. Using azimuthal seismic anisotropy, we can thus infer the age-dependent thickness of the mechanically defined rigid oceanic lithosphere and, furthermore, examine the depth extent of the low-viscosity, high strain-rate asthenosphere (Nishimura & Forsyth 1989; Smith *et al.* 2004; Debayle & Ricard 2013; Beghein *et al.* 2014).

Absolute plate motion models provide a means for comparing kinematic motions derived from diverse geological or geophysical data sets to a fixed reference frame. The selection of the reference frame, however, is itself subjective, with different reference frames

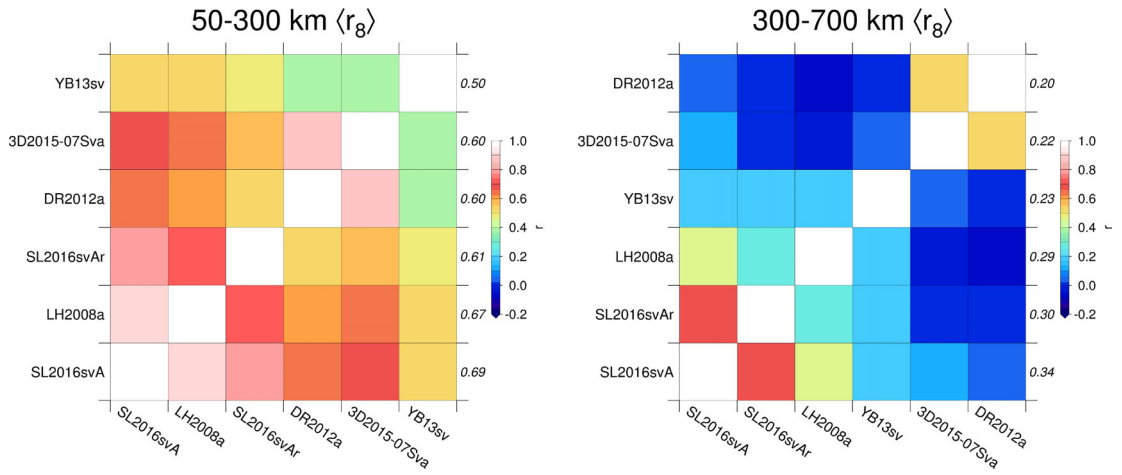

Figure 13. Comparison of radially averaged intermodel correlations for global, upper-mantle anisotropy models, up to and including degree 8 ($\langle r_8 \rangle$). The left panel illustrates correlations for the upper mantle at 50–300 km depths; the right panel shows the correlations for the depth range 300–700 km. In each panel, the models are sorted (left-right, bottom-up) by the decreasing total correlation (excluding autocorrelation, the white squares along the diagonal); these values are shown along the right vertical axis of each panel. Note that the sorting of the models differs between the two depth ranges.

resulting in a variety of absolute plate motion models with differing degrees of net rotation of the lithosphere (with respect to a fixed lower mantle). The inferred flow orientations are often interpreted in terms of the LPO of anisotropic minerals induced by shearing within the lithospheric and asthenospheric mantle. In the upper mantle, this is commonly assumed to be associated with an A-type olivine fabric, where the fast direction is parallel to mantle flow (Long & Becker 2010). However, in regions where a different fabric may dominate, such as an olivine B-type (Long & Becker 2010; Jung & Karato 2001), or where flow may be subvertical, the inferred fast direction may no longer be parallel to mantle flow.

Using two new absolute plate motion reference frames derived in Becker *et al.* (2015), we re-examine and re-iterate the results of Becker *et al.* (2014) in Fig. 14. Here we plot the misfit ($\langle \Delta\alpha \rangle$) of SL2016svA with predictions of four different APM models: Pal-Spr, FM-LPO, SA-APM and Sani-APM. The palaeospreading (Pal-Spr) model of frozen-in shear orientations in the oceanic lithosphere is derived by taking the gradient of the seafloor age (e.g. Conrad & Lithgow-Bertelloni 2007; Becker *et al.* 2014). The mantle flow model (FM-LPO) of Becker *et al.* (2008) relates mantle flow to anisotropic fabrics by means of predicting the synthetic LPO of olivine. The spreading-aligned plate motion model (SA-APM) describes current plate motions in a new, generalized reference frame (Becker *et al.* 2015). It was derived by minimizing the misfit between absolute plate motions in the no net rotation (NNR) reference MORVEL56-NNR (Argus *et al.* 2011) and seafloor spreading orientations. The fourth model is an optimized seismic anisotropy aligned reference frame (Sani-APM) tuned to minimize the angular misfit between plate motions (using MORVEL56-NNR; Argus *et al.* 2011) and the fast directions of SL2016svA at 150 km depth (*cf.* Montagner & Anderson 2015). (We note that the Euler poles of the net rotation of the lithosphere calculated for the latter two models and the equivalent anisotropy aligned poles computed for DR2012a and YB13sv are similar, as shown by Becker *et al.* (2015).)

In examining the mean angular misfits, a value 20° can be considered a very good match. At depths shallower than ∼110–125 km, the misfit is lowest for the palaeospreading (Pal-Spr, dark blue) model (left panel). This represents the shearing orientations frozen into the oceanic lithosphere as the plates were formed at mid-ocean ridges. Below this depth, the misfit of SL2016svA orientations with respect to Pal-Spr increases, indicating a worsening match with depth.

The remaining three models, in contrast, show the smallest misfits at sublithospheric depths. Their misfit with azimuthal anisotropy reaches a minimum at 150–200 km depths. The SA-APM and Sani-APM models yield a further 25 per cent reduction in average angular misfit compared to the misfit given by the FM-LPO model (Becker *et al.* 2014), dropping from ∼20° to only ∼15°.

The depth of the transition from where the misfits are minimized by the palaeospreading orientations to where they are minimized by plate motion or mantle flow models is observed at ∼115 km in left panel of Fig. 14; this transition likely marks the average boundary depth between the mechanically strong oceanic lithosphere and the underlying low-viscosity asthenosphere. Above this boundary, seismic anisotropy likely measures the orientation of fabrics frozen in at the time of plate formation, whereas beneath it seismic anisotropy is related to shearing within the weak asthenosphere, associated with the current or geologically recent plate motions (assuming an A-type olivine LPO fabric Debayle & Ricard 2013; Burgos *et al.* 2014).

The right-hand panels in Fig. 14 show the angular misfit between SL2016svA and the four absolute plate motion models as a function of depth and seafloor age. The average angular misfit (displayed bottom-left) is the total oceanic average weighted by the amplitude of anisotropy in SL2016svA. The thin dotted black line is the $\langle \Delta\alpha \rangle = 30°$ contour. Averaging of seafloor age is carried out in 5 Myr increments using bins 10 Myr in width. The superimposed 600 and 1200 °C half-space cooling isotherms were computed assuming a temperature-dependent conductivity (Xu *et al.* 2004) and asthenospheric temperature of 1315 °C (McKenzie *et al.* 2005).

The FM-LPO model (Becker *et al.* 2008) and the two new optimized reference frames, SA-APM and Sani-APM, all show a very low misfit region across the entire age-range. The upper boundary of this low-misfit region deepens as a function of age, so that the $\langle \Delta\alpha \rangle = 30°$ contour closely follows the 1200 °C isotherm. This strong contrast in angular misfit across the 1200 °C isotherm thus appears to define the boundary between the oceanic lithosphere and asthenosphere, deepening with age. Although thicker, this is in rough agreement with the lithospheric thickness variations estimated from azimuthal anisotropy

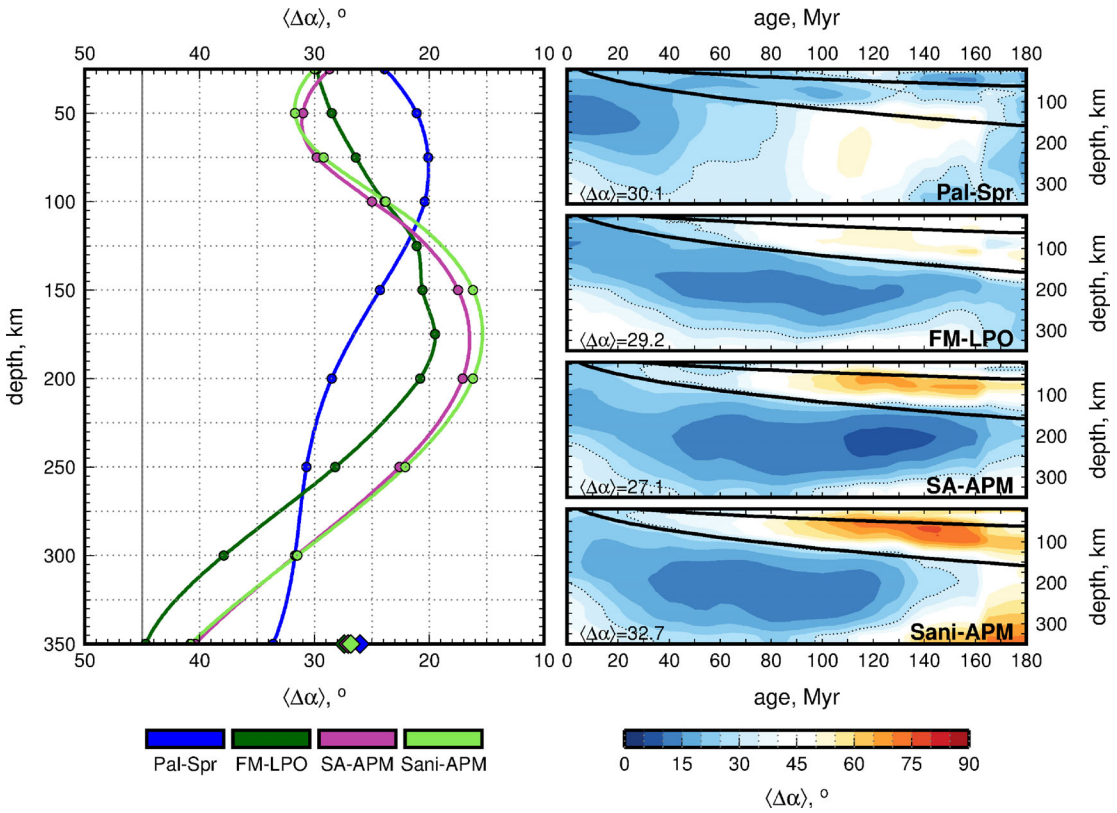

Figure 14. Angular misfits ($\langle\Delta\alpha\rangle$) of depth-dependent azimuthal anisotropy in SL2016svA with respect to four models providing different proxies for mantle flow: Pal-Spr (palaeospreading; blue, Conrad & Lithgow-Bertelloni 2007; Becker *et al.* 2014), FM-LPO (green, the mantle flow model of Becker *et al.* 2008), SA-APM (purple, the spreading-aligned current plate motion model in the universal reference frame derived by Becker *et al.* 2015) and Sani-APM (light-green, the current plate motion model in a reference frame such that orientations of seismic anisotropy in SL2016svA at 150 km depth are minimized; Becker *et al.* 2015). Depth-invariant models Pal-Spr, SA-APM and Sani-APM were projected downwards across the depth range. Left panel shows the vertical misfit profile averaged over all ocean basins, and weighted by the SL2016svA anisotropy amplitude. The filled diamonds along the bottom axis denote the total vertical average across the 50–350 km depth range. The light grey line at $\langle\Delta\alpha\rangle = 45^\circ$ indicates a random average orientation between the two models. The right-hand panels show the angular misfit variations as a function of seafloor age and depth. The solid black lines denote the 600° (upper) and 1200° (lower) half space cooling isotherms, whereas the dotted black line denotes the $\langle\Delta\alpha\rangle = 30^\circ$ contour. The average misfit in each panel is indicated in the lower left corners.

by Debayle & Ricard (2013), Beghein *et al.* (2014) and Burgos *et al.* (2014), who estimated the thermal thickness to coincide with the 1100 °C, 900–1100 °C and ∼1100–1200 °C isotherms, respectively.

The lower boundary of the low-misfit region does not show a dependence on plate age, apart from oceans younger than ∼40 Myr. This deeper boundary may correspond to the base of the low-viscosity asthenosphere at around 300 km depth (although the possibility of a change in the nature of LPO formation in the deep upper mantle (Mainprice *et al.* 2005) would add an interesting twist to interpretation of these data and warrant a further investigation in the future).

The thermal structure of the oceanic lithosphere is controlled, to first order, by the half-space cooling model (Davis & Lister 1974; McKenzie *et al.* 2005). However, the apparent lack of heat-flow dependence on lithospheric age for oceans older than (∼80 Myr), as well as the flattening of the old oceans' bathymetry, have motivated the development of an alternative, plate model, in which the plate thickness remains constant for oceans older than ∼80 Myr (Stein & Stein 1992; Korenaga 2015; Stein & Stein 2015). Interestingly, seismic anisotropy (Fig. 14) suggests that the mechanical lithosphere does continue to thicken with depth up to the oldest oceans' ages, with the deepening of the lithosphere-asthenosphere boundary closely following a half-space cooling isotherm (*cf.* Becker *et al.* 2014).

Within continental regions, where the tectonic history is vastly more complex than beneath ocean basins, simple analysis of anisotropy as a function of age is not feasible. For instance, should the 'age' of a given region reflect the crustal age or, instead, the age when the lithosphere is thought to have been altered last? Despite these challenges, the insights gained from relatively simple oceanic domains can still be applied to our understanding of the continental interiors. For instance, given that the depth to the mechanical LAB shows a temperature dependence, a similar minimum angular misfit in seismic anisotropy with respect to plate motion may be observed. It is not uncommon that seismic anisotropy in the lithosphere is not aligned with the current plate motion, and a strong contrast in angular misfit has indeed observed in various locations, for example beneath North America (Yuan *et al.* 2011) or Australia (Debayle *et al.* 2005).

9 CONCLUSIONS

We have introduced two versions of a new, global model of azimuthal anisotropy of the vertically polarized shear velocity in the upper mantle. The models SL2016svA and SL2016svAr are constrained by a very large data set of waveform fits, the same as was used to compute the isotropic component of the high-resolution global anisotropic shear-velocity model SL2013sv

(Schaeffer & Lebedev 2013, 2015). The amplitudes recovered in both of our models are higher than those in most past global models of azimuthal anisotropy. The exceptions are the recently published DR2012a and 3D2015-07Sva, which attain localized higher amplitudes. SL2016svA and SL2016svAr show a pronounced decrease in the amplitude of anisotropy with increasing depth below 150–200 km depth, consistent with other global models (Lebedev & van der Hilst 2008; Ekström 2011; Debayle & Ricard 2013; Yuan & Beghein 2013). Quantitative comparison between recent seismic anisotropy models demonstrates that they are correlated most strongly in the upper mantle (50–300 km) and are much more poorly correlated in the transition zone.

With the inclusion of several dense regional seismic networks into our data set, fine-scale patterns of anisotropy are detected in well-sampled continental regions. Within the Tibetan Plateau, for example, we resolve anisotropy formed by west-east oriented crustal flow, which rotates around the Eastern Himalayan Syntaxis. Beneath the western United States, another continental region undergoing active continental deformation, lateral and vertical contrasts in the orientation of the fast-axis of wave propagation are seen clearly. In the shallow lithosphere, the fast-propagation directions beneath the western US are different from those in the Pacific Ocean adjacent to the west and the stable cratonic interior adjacent to the east. At greater depth within the deforming margin, the fast direction rotates to more closely match that in the Pacific Ocean.

The comparison of seismic anisotropy orientations with proxies for past and present plate motion enables the determination of the depth to the top of the mechanically weak, low-viscosity asthenosphere. Beneath oceanic regions, with typically longer wavelength patterns of seismic anisotropy, we use the fit of the depth-dependent anisotropy with predictions from a global mantle circulation model and with directions of current plate motions to determine the age dependence of the depth of the mechanical LAB. The thus determined LAB depth closely follows the 1200 °C half-space cooling isotherm.

ACKNOWLEDGEMENTS

Waveform data were obtained from the facilities of the Incorporated Research Institutions for Seismology (IRIS), the Observatories and Research Facilities for European Seismology (ORFEUS), the GFZ Seismological Data Archive, and the Canadian National Seismic Network (CNSN). This manuscript was improved by insightful and constructive feedback from Caroline Beghein and Eric Debayle. We are grateful to the operators and PIs of the many networks used in this study, as well as the researchers who make their models freely available (in particular Caroline Beghein and Eric Debayle). This work was supported by Science Foundation Ireland (grants 09/RFP/GEO2550, 11/SIRG/E2174 and 13/CDA/2192) and the Natural Sciences and Engineering Research Council (NSERC) of Canada. All figures were generated using Generic Mapping Tools (GMT; Wessel & Smith 1995). Our tomographic models, SL2016svA and SL2016svAr, can be obtained from *http://andrewjschaeffer.wordpress.com/Models/SL2016svA.html*.

REFERENCES

Adam, J.M.-C. & Lebedev, S., 2012. Azimuthal anisotropy beneath southern Africa from very broad-band surface-wave dispersion measurements, *Geophys. J. Int.,* **191**(1), 155–174.

Agius, M.R., 2012. The structure and dynamics of the lithosphere beneath Tibet from seismic surface-wave analysis, *PhD thesis,* Trinity College, Dublin, Unversity.

Agius, M.R. & Lebedev, S., 2014. Shear-velocity structure, radial anisotropy and dynamics of the Tibetan crust, *Geophys. J. Int.,* **199,** 1395–1415.

Anderson, D.L., 1989. *Theory of the Earth,* Blackwell Scientific Publications.

Argus, D.F., Gordon, R.G. & DeMets, C., 2011. Geologically current motion of 56 plates relative to the no-net-rotation reference frame, *Geochem. Geophys. Geosyst.,* **12**(11), 1–13.

Auer, L., Boschi, L., Becker, T.W., Nissen-Meyer, T. & Giardini, D., 2014. Savani: a variable resolution whole-mantle model of anisotropic shear velocity variations based on multiple datasets, *J. geophys. Res.,* **119,** 3006–3034.

Babuska, V. & Cara, M., 1991. *Seismic Anisotropy in the Earth,* Kluwer Academic Press.

Barruol, G., Silver, P.G. & Vauchez, A., 1997. Seismic anisotropy in the eastern United States: deep structure of a complex continental plate, *J. geophys. Res.,* **102,** 8329–8348.

Bassin, C., Laske, G. & Masters, G., 2000. The current limits of resolution for surface wave tomography in North America, *EOS, Trans. Am. geophys. Un.,* **81,** F897.

Bastow, I.D., Thompson, D.a., Wookey, J., Kendall, J.M., Helffrich, G., Snyder, D.B., Eaton, D.W. & Darbyshire, F.A., 2011. Precambrian plate tectonics: seismic evidence from Northern Hudson Bay, Canada, *Geology,* **39**(1), 91–94.

Becker, T.W. & Boschi, L., 2002. A comparison of tomographic and geodynamic mantle models, *Geochem. Geophys. Geosyst.,* **3,** doi:10.129/2001GC000168.

Becker, T.W., Ekström, G., Boschi, L. & Woodhouse, J.H., 2007. Length scales patterns, and origin of azimuthal seismic anisotropy in the upper mantle as mapped by Rayleigh waves, *Geophys. J. Int.,* **171**(1), 451–462.

Becker, T.W., Kustowski, B. & Ekström, G., 2008. Radial seismic anisotropy as a constraint for upper mantle rheology, *Earth planet. Sci. Lett.,* **267**(1–2), 213–227.

Becker, T.W., Lebedev, S. & Long, M.D., 2012. On the relationship between azimuthal anisotropy from shear wave splitting and surface wave tomography, *J. geophys. Res.,* **117**(B1), 1–17.

Becker, T.W., Conrad, C.P., Schaeffer, A.J. & Lebedev, S., 2014. Origin of azimuthal seismic anisotropy in oceanic plates and mantle, *Earth planet. Sc. Lett.,* **401,** 236–250.

Becker, T.W., Schaeffer, A.J., Lebedev, S. & Conrad, C.P., 2015. Toward a generalized plate motion reference frame, *Geophys. Res. Lett.,* **42**(9), 3188–3196.

Beghein, C. & Trampert, J., 2004. Probability density functions for radial anisotropy: Implications for the upper 1200 km of the mantle, *Earth planet. Sc. Lett.,* **217**(1–2), 151–162.

Beghein, C., Yuan, K., Schmerr, N. & Xing, Z., 2014. Changes in seismic anisotropy shed light on the nature of the Gutenberg discontinuity, *Science,* **343**(6176), 1237–1240.

Beucler, É. & Montagner, J.-P., 2006. Computation of Large Anisotropic Seismic Heterogeneities (CLASH), *Geophys. J. Int.,* **165**(2), 447–468.

Boschi, L. & Woodhouse, J.H., 2006. Surface wave ray tracing and azimuthal anisotropy: a generalized spherical harmonic approach, *Geophys. J. Int.,* **164**(3), 569–578.

Burgos, G., Montagner, J.-P., Beucler, E., Capdeville, Y., Mocquet, A. & Drilleau, M., 2014. Oceanic lithosphere-asthenosphere boundary from surface wave dispersion data, *J. geophys. Res.,* **119**(2), 1079–1093.

Cara, M. & Lévêque, J.-J., 1987. Waveform inversion using secondary observables, *Geophys. Res. Lett.,* **14,** 1046–1049.

Chang, S.J., Ferreira, A.M., Ritsema, J., van Heijst, H.J. & Woodhouse, J.H., 2014. Global radially anisotropic mantle structure from multiple datasets: a review, current challenges, and outlook, *Tectonophysics,* **617,** 1–19.

Chang, S.J., Ferreira, A.M., Ritsema, J., van Heijst, H.J. & Woodhouse, J.H., 2015. Joint inversion for global isotropic and radially anisotropic mantle structure including crustal thickness perturbations, *J. geophys. Res.,* **120,** 4278–4300.

Conrad, C.P. & Lithgow-Bertelloni, C., 2007. Faster seafloor spreading and lithosphere production during the mid-Cenozoic, *Geology,* **35**(1), 29–32.

Currie, C.A., Cassidy, J.F., Hyndman, R.D. & Bostock, M.G., 2004. Shear wave anisotropy beneath the Cascadia subduction zone and western North American craton, *Geophys. J. Int.,* **157**(1), 341–353.

Darbyshire, F.A. & Lebedev, S., 2009. Rayleigh wave phase-velocity heterogeneity and multilayered azimuthal anisotropy of the Superior Craton, Ontario, *Geophys. J. Int.,* **176,** 215–234.

Davis, E.E. & Lister, C.R.B., 1974. Fundamentals of ridge crest topography, *Earth planet. Sci. Lett.,* **21,** 405–413.

Debayle, E. & Ricard, Y., 2012. A global shear velocity model of the upper mantle from fundamental and higher Rayleigh mode measurements, *J. geophys. Res.,* **117**(B10), 1–24.

Debayle, E. & Ricard, Y., 2013. Seismic observations of large-scale deformation at the bottom of fast-moving plates, *Earth planet. Sci. Lett.,* **376,** 165–177.

Debayle, E., Kennett, B.L.N. & Priestley, K., 2005. Global azimuthal seismic anisotropy and the unique plate-motion deformation of Australia, *Nature,* **433**(7025), 509–512.

Debayle, E., Dubuffet, F. & Durand, S., 2016. An automatically updated s-wavemodel of the upper mantle and the depth extent of azimuthal anisotropy, *Geophys. Res. Lett.,* **43,** 1–8.

Deschamps, F., Lebedev, S., Meier, T. & Trampert, J., 2008a. Stratified seismic anisotropy reveals past and present deformation beneath the East-central United States, *Earth planet. Sci. Lett.,* **274**(3–4), 489–498.

Deschamps, F., Lebedev, S., Meier, T. & Trampert, J., 2008b. Azimuthal anisotropy of Rayleigh-wave phase velocities in the east-central United States, *Geophys. J. Int.,* **173**(3), 827–843.

Dziewonski, A.M. & Anderson, D.L., 1981. Preliminary reference Earth model, *Phys. Earth planet. Inter.,* **25,** 297–356.

Eakin, C.M., Obrebski, M., Allen, R.M., Boyarko, D.C., Brudzinski, M.R. & Porritt, R., 2010. Seismic anisotropy beneath Cascadia and the Mendocino triple junction: interaction of the subducting slab with mantle flow, *Earth planet. Sci. Lett.,* **297**(3–4), 627–632.

Eaton, D., Frederiksen, A. & Miong, S.K., 2004. Shear-wave splitting observations in the lower Great Lakes region: evidence for regional anisotropic domains and keel-modified asthenospheric flow, *Geophys. Res. Lett.,* **31**(7), 2000–2003.

Ekström, G., 2006. A simple method of representing azimuthal anisotropy on a sphere, *Geophys. J. Int.,* **165**(2), 668–671.

Ekström, G., 2011. A global model of Love and Rayleigh surface wave dispersion and anisotropy, 25–250 s, *Geophys. J. Int.,* **187,** 1668–1686.

Ekström, G., Nettles, M. & Dziewónski, A.M., 2012. The global CMT project 2004–2010: Centroid-moment tensors for 13,017 earthquakes, *Phys. Earth planet. Inter.,* **200–201,** 1–9.

Endrun, B., Lebedev, S., Meier, T., Tirel, C. & Friederich, W., 2011. Complex layered deformation within the Aegean crust and mantle revealed by seismic anisotropy, *Nat. Geosci.,* **4**(3), 203–207.

Forsyth, D.W., 1975. The early structural evolution and anisotropy of the oceanic upper mantle, *Geophys. J. R. astr. Soc.,* **43,** 103–162.

Fouch, M.J., 2003. Upper-mantle anisotropy database. Available at: http://geophysics.asu.edu/anisotropy/upper/.

Fouch, M.J., Fischer, K.M., Parmentier, E.M., Wysession, M.E. & Clarke, T.J., 2000. Shear wave splitting, continental keels, and patterns of mantle flow, *J. geophys. Res.,* **105**(B3), 6255–6275.

French, S., Lekic, V. & Romanowicz, B., 2013. Waveform tomography reveals channeled flow at the base of the oceanic asthenosphere, *Science,* **342**(6155), 227–230.

Gaherty, J.B. & Jordan, T.H., 1995. Lehmann discontinuity as the base of an anisotropic layer beneath continents, *Science,* **268**(5216), 1468–1471.

Gripp, A.E. & Gordon, R.G., 2002. Young tracks of hotspots and current plate velocities, *Geophys. J. Int.,* **150,** 321–361.

Hess, H.H., 1964. Seismic anisotropy of the uppermost mantle under oceans, *Nature,* **203,** 629–631.

Hongsresawat, S., Panning, M.P., Russo, R.M., Foster, D.A., Monteiller, V. & Chevrot, S., 2015a. USArray shear wave splitting shows seismic anisotropy from both lithosphere and asthenosphere, *Geology,* **43**(8), 1–4.

Hongsresawat, S., Panning, M.P., Russo, R.M., Foster, D.A., Monteiller, V. & Chevrot, S., 2015b. USArray shear wave splitting shows seismic anisotropy from both lithosphere and asthenosphere, *Geology,* **43**(8), 667–670.

Jung, H. & Karato S, 2001. Water-induced fabric transitions in olivine, *Science,* **293**(5534), 1460–1463.

Karato, S.-I., 1992. On the Lehmann discontinuity, *Geophys. Res. Lett.,* **19**(22), 2255–2258.

Karato, S.-I., Jung, H., Katayama, I. & Skemer, P., 2008. Geodynamic Significance of Seismic Anisotropy of the upper mantle: new insights from laboratory studies, *Annu. Rev. Earth Planet. Sci.,* **36**(1), 59–95.

Kennett, B.L.N., Engdahl, E.R. & Buland, R., 1995. Constraints on seismic velocities in the Earth from traveltimes, *Geophys. J. Int.,* **122**(1), 108–124.

Korenaga, J., 2015. Seafloor topography and the thermal budget of the Earth, *Geol. Soc. Am. Spec. Pap.,* **514** (SPE514-11), 167–185.

Kustowski, B., Ekström, G. & Dziewónski, A.M., 2008. Anisotropic shear-wave velocity structure of the Earth's mantle: a global model, *J. geophys. Res.,* **113**(B6), 1–23.

Lebedev, S. & van der Hilst, R.D., 2008. Global upper-mantle tomography with the automated multimode inversion of surface and S-wave forms, *Geophys. J. Int.,* **173,** 505–518.

Lebedev, S., Nolet, G., Meier, T. & van der Hilst, R.D., 2005. Automated multimode inversion of surface and S waveforms, *Geophys. J. Int.,* **162,** 951–964.

Lebedev, S., Boonen, J. & Trampert, J., 2009. Seismic structure of Precambrian lithosphere: new constraints from broad-band surface-wave dispersion, *Lithos,* **109,** 96–111.

Levin, V., Menke, W. & Lerner-Lam, A., 1996. Seismic anisotropy in the north-eastern US as a source of significant teleseismic P traveltime anomalies, *Geophys. J. Int.,* **126**(2), 593–603.

Lin, F.-C., Ritzwoller, M.H., Yang, Y., Moschetti, M.P. & Fouch, M.J., 2010. Complex and variable crustal and uppermost mantle seismic anisotropy in the western United States, *Nat. Geosci.,* **4**(1), 55–61.

Long, M.D. & Becker, T.W., 2010. Mantle dynamics and seismic anisotropy, *Earth planet. Sci. Lett.,* **297**(3–4), 341–354.

Ma, Z. & Masters, G., 2015. Effect of earthquake locations on Rayleigh wave azimuthal anisotropy models, *Geophys. J. Int.,* **203,** 1319–1333.

Maggi, A., Debayle, E., Priestley, K. & Barruol, G., 2006. Multimode surface waveform tomography of the Pacific Ocean: a closer look at the lithospheric cooling signature, *Geophys. J. Int.,* **166**(3), 1384–1397.

Mainprice, D., 2007. Seismic anisotropy of the deep Earth from a mineral and rock physics perspective, *Treatise Geophys.,* **2,** 437–491.

Mainprice, D., Tommasi, A., Couvy, H., Cordier, P. & Frost, D.J., 2005. Pressure sensitivity of olivine slip systems and seismic anisotropy of Earth's upper mantle, *Nature,* **433**(7027), 731–733.

Marone, F. & Romanowicz, B., 2007. Non-linear crustal corrections in high-resolution regional waveform seismic tomography, *Geophys. J. Int.,* **170**(1), 460–467.

Marone, F., Gung, Y. & Romanowicz, B., 2007. Three-dimensional radial anisotropic structure of the North American upper mantle from inversion of surface waveform data, *Geophys. J. Int.,* **171**(1), 206–222.

McKenzie, D., Jackson, J.A. & Priestley, K., 2005. Thermal structure of oceanic and continental lithosphere, *Earth planet. Sci. Lett.,* **233**(3–4), 337–349.

Meschede, M. & Romanowicz, B., 2015. Lateral heterogeneity scales in regional and global upper mantle shear velocity models, *Geophys. J. Int.,* **200,** 1076–1093.

Montagner, J. & Anderson, D.L., 2015. The Pacific Megagash: a future plate boundary?, in *The Don L Anderson Honourary Volume,* pp. 1–24, ed. Fougler, G.L., Geol. Soc. Am.

Montagner, J.-P. & Anderson, D.L., 1989. Petrological constraints on seismic anisotropy, *Phys. Earth planet. Inter.,* **54,** 82–105.

Montagner, J.-P. & Guillot, L., 2002. Seismic anisotropy and global geodynamics, *Rev. Mineral. Geochem.,* **51**(1), 353–385.

Montagner, J.-P. & Kennett, B.L.N., 1996. How to reconcile body-wave and normal-mode reference earth models, *Geophys. J. Int.,* **125**(1), 229–248.

Montagner, J.-P. & Tanimoto, T., 1991. Global upper mantle tomography of seismic velocities and anisotropies, *J. geophys. Res.,* **96**(B12), 20 337–20 351.

Moulik, P. & Ekstrom, G., 2014. An anisotropic shear velocity model of the Earth's mantle using normal modes, body waves, surface waves and long-period waveforms, *Geophys. J. Int.,* **199**(3), 1713–1738.

Nelson, K.D. *et al.*, 1996. Partially molten middle crust beneath southern Tibet: synthesis of project INDEPTH results, *Science,* **274**(5293), 1684–1688.

Nishimura, C.E. & Forsyth, D.W., 1989. The anisotropic structure of the upper mantle in the Pacific, *Geophys. J. Int.,* **96**(2), 203–229.
Nolet, G., 1990. Partitioned waveform inversion and two-dimensional structure under the network of autonomously recording seismographs, *J. geophys. Res.,* **95**(B6), 8499–8512.
Pandey, S., Yuan, X., Debayle, E., Tilmann, F., Priestley, K. & Li, X., 2015. Depth-variant azimuthal anisotropy in Tibet revealed by surface wave tomography, *Geophys. Res. Lett.,* **42,** 4326–4334.
Panning, M.P. & Romanowicz, B., 2006. A three-dimensional radially anisotropic model of shear velocity in the whole mantle, *Geophys. J. Int.,* **167**(1), 361–379.
Phinney, R.A. & Burridge, R., 1973. Representation of the elasticgravitational excitation of a spherical earth model by generalized spherical harmonics, *Geophys. J. R. astr. Soc.,* **34,** 451–487.
Polat, G., Lebedev, S., Readman, P.W., O'Reilly, B.M. & Hauser, F., 2012. Anisotropic Rayleigh-wave tomography of Ireland's crust: implications for crustal accretion and evolution within the Caledonian Orogen, *Geophys. Res. Lett.,* **39**(4), 1–5.
Roux, E., Moorkamp, M., Jones, A.G., Bischoff, M., Endrun, B., Lebedev, S. & Meier, T., 2011. Joint inversion of long-period magnetotelluric data and surface-wave dispersion curves for anisotropic structure: application to data from Central Germany, *Geophys. Res. Lett.,* **38**(5), 1–5.
Schaeffer, A. & Lebedev, S., 2014. Imaging the North American continent using waveform inversion of global and USArray data, *Earth planet. Sci. Lett.,* **402,** 26–41.
Schaeffer, A.J. & Lebedev, S., 2013. Global shear speed structure of the upper mantle and transition zone, *Geophys. J. Int.,* **194**(1), 417–449.
Schaeffer, A.J. & Lebedev, S., 2015. Global heterogeneity of the lithosphere and underlying mantle: a seismological appraisal based on multimode surface-wave dispersion analysis, shear-velocity tomography, and tectonic regionalization, in *The Earth's Heterogeneous Mantle,* pp. 3–46, eds Khan, A. & Deschamps, F., Springer.
Silver, P.G., 1996. Seismic anisotropy beneath the continents: Probing the depths of geology, *Annu. Rev. Earth Planet. Sci.,* **24,** 385–432.
Simons, F.J., van der Hilst, R.D., Montagner, J.-P. & Zielhuis, A., 2002. Multimode Rayleigh wave inversion for heterogeneity and azimuthal anisotropy of the Australian upper mantle, *Geophys. J. Int.,* **151**(3), 738–754.
Smith, D.B., Ritzwoller, M.H. & Shapiro, N.M., 2004. Stratification of anisotropy in the Pacific upper mantle, *J. geophys. Res.,* **109**(B11), 1–22.
Smith, M.L. & Dahlen, F.A., 1973. The azimuthal dependence of Love and Rayleigh wave propagation in a slightly anisotropic medium, *J. geophys. Res.,* **78**(17), 3321–3333.
Sodoudi, F., Yuan, X., Kind, R., Lebedev, S., Adam, J. M.-C., Kästle, E. & Tilmann, F., 2013. Seismic evidence for stratification in composition and anisotropic fabric within the thick lithosphere of Kalahari Craton, *Geochem. Geophys. Geosyst.,* **14**(12), 5393–5412.
Stein, C. & Stein, S., 1992. A model for the global variation in oceanic depth and heat flow with lithospheric age, *Nature,* **359,** 123–129.
Stein, C.A. & Stein, S., 2015. Are large oceanic depth anomalies caused by thermal perturbations?, in *The Interdisciplinary Earth: A Volume in Honor of Don L. Anderson: Geological Society of America Special Paper 514 and American Geophysical Union Special Publication 71,* eds Foulger, G., Lustrino, M. & King, S., doi:10.1130/2015.2514(12).
Tanimoto, T. & Anderson, D.L., 1984. Mapping convection in the mantle, *Geophys. Res. Lett.,* **11**(4), 287–290.
Trampert, J. & van Heijst, H.J., 2002. Global azimuthal anisotropy in the transition zone, *Science,* **296**(5571), 1297–1299.
Trampert, J. & Woodhouse, J.H., 2003. Global anisotropic phase velocity maps for fundamental mode surface waves between 40 and 150 s, *Geophys. J. Int.,* **154,** 154–165.
Visser, K., Lebedev, S., Trampert, J. & Kennett, B.L.N., 2007. Global Love wave overtone measurements, *Geophys. Res. Lett.,* **34**(3), 1–6.
Visser, K., Trampert, J. & Kennett, B.L.N., 2008a. Global anisotropic phase velocity maps for higher mode Love and Rayleigh waves, *Geophys. J. Int.,* **172**(3), 1016–1032.
Visser, K., Trampert, J., Lebedev, S. & Kennett, B., 2008b. Probability of radial anisotropy in the deep mantle, *Earth planet. Sci. Lett.,* **270**(3–4), 241–250.
Wang, Z. & Dahlen, F.A., 1995. Spherical-spline parameterization of three-dimensional Earth models, *Geophys. Res. Lett.,* **22**(22), 3099–3102.
Wessel, P. & Smith, W., 1995. New version of the Generic Mapping Tools released, *EOS, Trans. Am. geophys. Un.,* **76,** 329.
Wüstefeld, A., Bokelmann, G., Barruol, G. & Montagner, J.-P., 2009. Identifying global seismic anisotropy patterns by correlating shear-wave splitting and surface-wave data, *Phys. Earth planet. Inter.,* **176**(3–4), 198–212.
Xu, Y. *et al.*, 2004. Thermal diffusivity and conductivity of olivine, wadsleyite and ringwoodite to 20 GPa, *Phys. Earth planet. Inter.,* **143**(1–2), 321–336.
Yang, Y. & Forsyth, D.W., 2006. Rayleigh wave phase velocities, small-scale convection, and azimuthal anisotropy beneath southern California, *J. geophys. Res.,* **111**(B7), 1–20.
Yang, Y., Zheng, Y. & Ritzwoller, M.H., 2010. Rayleigh-wave phase velocities and azimuthal anisotropy in Tibet and surrounding regions from ambient noise tomography, in *Proceedings of the 25th Himalaya-Karakoram-Tibet Workshop,* US Geological Survey Open File Report, 2010-1099.
Yao, H., van der Hilst, R.D. & de Hoop, M.V., 2006. Surface-wave array tomography in SE Tibet from ambient seismic noise and two-station analysis—I. Phase velocity maps, *Geophys. J. Int.,* **166**(2), 732–744.
Yuan, H., Romanowicz, B., Fischer, K.M. & Abt, D.L., 2011. 3-D shear wave radially and azimuthally anisotropic velocity model of the North American upper mantle, *Geophys. J. Int.,* **184**(3), 1237–1260.
Yuan, K. & Beghein, C., 2013. Seismic anisotropy changes across upper mantle phase transitions, *Earth planet. Sci. Lett.,* **374,** 132–144.
Yuan, K. & Beghein, C., 2014. Three-dimensional variations in Love and Rayleigh wave azimuthal anisotropy for the upper 800 km of the mantle, *J. geophys. Res.,* **119**(4), 3232–3255.
Zhang, X., Paulssen, H., Lebedev, S. & Meier, T., 2007. Surface wave tomography of the Gulf of California, *Geophys. Res. Lett.,* **34**(15), 1–5.
Zhang, X., Paulssen, H., Lebedev, S. & Meier, T., 2009. 3D shear velocity structure beneath the Gulf of California from Rayleigh wave dispersion, *Earth planet. Sci. Lett.,* **279**(3–4), 255–262.
Zhu, H. & Tromp, J., 2013. Mapping tectonic deformation in the crust and upper mantle beneath Europe and the North Atlantic Ocean, *Science,* **341**(6148), 871–875.

SUPPORTING INFORMATION

Additional Supporting Information may be found in the online version of this paper:

Table S1. Level of significance between the radially averaged correlation coefficients contained in Table 1 for the depth range 50–700 km, computed following the method of Becker *et al.* (2007). The upper half of the table is for $\langle r_8 \rangle$ and the lower half is for $\langle r_{20} \rangle$.
Table S2. Level of significance between the radially averaged correlation coefficients contained in Table 1 for the depth range 50–300 km, computed following the method of Becker *et al.* (2007). The upper half of the table is for $\langle r_8 \rangle$ and the lower half is for $\langle r_{20} \rangle$.
Table S3. Level of significance between the radially averaged correlation coefficients contained in Table 1 for the depth range 300–700 km, computed following the method of Becker *et al.* (2007). The upper half of the table is for $\langle r_8 \rangle$ and the lower half is for $\langle r_{20} \rangle$.
Figure S1. Comparison of isotropic component of SL2016svA (top row, SL2013sv; Schaeffer & Lebedev (2013)) with the isotropic component of SL2016svAr (bottom row) at depths of 100, 250 and 500 km. Below each pair of panels, the saturation limits in percent are indicated, followed by the difference in RMS perturbations between each set of panels.
Figure S2. Synthetic tests illustrating the leakage between the isotropic and anisotropic model parameters. The results of two tests are illustrated at depths of 100, 250 and 500 km. The left panels illustrate the isotropic velocity anomalies that result

from the inversion of a synthetic dataset generated from a purely anisotropic model, whereas the right panels show the anisotropic structure resulting from the inversion of a synthetic dataset derived from an isotropic model. Colour scales are indicated beneath each set of panels. Saturation limits for isotropic velocity are denoted top left of each map. For both isotropic and anisotropic maps, the RMS perturbation in percent is denoted at bottom right.

Figure S3. Angular misfit of SL2016svA compared with five other azimuthal anisotropy models: SL2016svAr, LH2008a (Lebedev & van der Hilst 2008; Becker *et al*. 2012), YB13sv (Yuan & Beghein 2013), 3D2015-07Sva (Debayle *et al*. 2016) and DR2012a (Debayle & Ricard 2013), at depths of 50 km (left column), 100 km (centre column), and 200 km (right column). The colour scale indicates misfit in azimuthal anisotropy orientation between the models, with weighting based on the amplitude on SL2016svA. Global average angular misfit ($\langle\triangle\alpha\rangle$) is indicated at the lower left of each panel, with the continental ($\langle\triangle\alpha\rangle_c$) and oceanic ($\langle\triangle\alpha\rangle_o$) averages at lower right.

Figure S4. Average angular misfit $\langle\triangle\alpha\rangle$ of fast-propagation directions in seismic anisotropy models as a function of depth, with respect to SL2016svAr, LH2008a (Lebedev & van der Hilst 2008; Becker *et al*. 2012), DR2012a (Debayle & Ricard 2013), 3D2015-07Sva (Debayle *et al*. 2016) and YB13sv (Yuan & Beghein 2013). Solid curves: the global averages; dashed: for oceanic regions only; dash-dotted: continental regions only. Filled diamonds along the bottom axis indicate the depth-averaged global misfit for each model. Light grey line at $\langle\triangle\alpha\rangle = 45^\circ$ indicates a random average orientation between the two models. Note that the colours representing the different models change between the different panels.

Figure S5. Angular misfits between fast-propagation directions in tomographic models LH2008a (Lebedev & van der Hilst 2008; Becker *et al*. 2012), YB13sv (Yuan & Beghein 2013), 3D2015-07Sva (Debayle *et al*. 2016) and DR2012a (Debayle & Ricard 2013) with the global spherical harmonic expansion of *SKS* splitting distribution from Becker *et al*. (2012), for depths of 125 km (left column) and 250 km (right column). For both the tomographic models and *SKS* splitting, anisotropy was expanded in generalized spherical harmonics up to maximum angular degree 20. The colour scale indicates misfit in azimuthal anisotropy orientation between the models, with weighting based on the amplitude of the tomography model. Global average angular misfit ($\langle\triangle\alpha\rangle$) is indicated at the lower left of each panel, with the continental ($\langle\triangle\alpha\rangle_c$) and oceanic ($\langle\triangle\alpha\rangle_o$) averages at the lower right.

Figure S6. Comparison of radially averaged inter-model correlations for global, upper-mantle anisotropy models, up to and including degree 8 ($\langle r_8\rangle$). The left panel illustrates correlations for the upper mantle at 50–200 km depths; the right panel shows the correlations for the depth range 200–700 km. In each panel, the models are sorted (left-right, bottom-up) by the decreasing total correlation (excluding auto-correlation, the white squares along the diagonal); these values are shown along the right vertical axis of each panel. Note that the sorting of the models differs between the two depth ranges.

(http://gji.oxfordjournals.org/lookup/suppl/doi:10.1093/gji/ggw309/-/DC1)

Please note: Oxford University Press is not responsible for the content or functionality of any supporting materials supplied by the authors. Any queries (other than missing material) should be directed to the corresponding author for the paper.

APPENDIX A: ANISOTROPIC PARAMETRIZATION

A1 Mapping of azimuthal variations

The choice of model parametrization can add additional complications for the azimuthally anisotropic terms in comparison to isotropic ones. In particular, this is most relevant in global tomography in which polar regions are included within the model domain. In the classic spherical harmonic expansion, the $m = 0$ azimuthally dependent harmonic components become singular upon reaching the pole. One alternative method to adequately describe the tensor field everywhere simultaneously across the entire unit sphere is generalized spherical harmonics (Trampert & Woodhouse 2003; Boschi & Woodhouse 2006), which avoid this singularity at the poles.

We instead choose to parametrize the lateral variations in seismic velocities using a triangular grid of knots with an approximately equal interknot spacing laterally (Wang & Dahlen 1995). This local parametrization enables easier targeting of regional-scale structure globally; furthermore, it is inherently simple to co-register different grids, which facilitates efficient transformation between each. In our case, we generate a dense integration grid (∼28 km spacing) for the reference model and sensitivity kernels, and a coarser model grid (i.e. ∼280 km spacing) on which the 3-D velocity perturbations are solved.

Although the choice of a local parametrization holds many benefits, one must still account for certain effects at high latitudes. This is true both when mapping the source-station great-circle-paths (GCP) and when smoothing as a form of regularization during inversion. Specifically, an azimuth—whether this be the source-station GCP azimuth or the fast-direction orientation—is defined with respect to the local meridian. Due to this local definition of the coordinate axes, the local azimuths at neighbouring knots are generally different.

Ekström (2006) circumvents this complication in polar regions by adjusting the ray-path azimuth at each of the spline knots of his parametrization for a given ray path by defining a 'local parallel azimuth'. This approach was implemented by Ma & Masters (2015) in defining local azimuths at nodes within a block parametrization.

We instead use the approach of Lebedev & van der Hilst (2008) to compute an 'equivalent local azimuth' at each grid knot within the approximate Frésnel zone; although it is implemented in a more *ad-hoc* manner than that of Ekström (2006), it produces a similar result. For a path j, a reference point ($\theta^{(j,R)}$, $\phi^{(j,R)}$) is defined, such that it lies on the event-station GCP a distance $\pi/2$ from the event-station path midpoint.

We compute the equivalent local azimuth at each of the grid knots (θ_i, ϕ_i) within the Frésnel zone as the azimuth between the ith knot and the reference point ($\theta^{(j,R)}$, $\phi^{(j,R)}$). With this formulation, the path azimuth is correctly mapped to be parallel to subparallel to the azimuth of the closest point along the ray path. Additionally, the knot directly at the North Pole (and equivalently at the South Pole) also has a correctly mapped azimuth, avoiding the singularity associated with defining a local azimuth at a point where all azimuths point to the opposite pole.

The main difference between this formulation and that of Ekström (2006) is that our equivalent local azimuth at each of the i non-zero model knots is actually subparallel to the path azimuth (at the closest point to the path), instead of being strictly parallel. These minor variations in the local azimuth loosely imitate the shape of the approximate Frésnel zone, where the azimuths near ends of the path

bend slightly towards the station and event location. The bending of the paths is greater for longer path lengths, as the station location (or event location) approaches the reference point (or its antipode). Since our maximum path length does not exceed 16 000 km (minor arcs only), this effect is never strong.

A2 Inversion parametrization

We parametrize azimuthal anisotropy in terms of the vector components A_1 and A_2 representing the π-periodic angular dependencies of the wave speed, as in eq. (1). Since the tomographic inverse problem is mixed-determined, we impose regularization conditions on the solution in order to stabilize the inversion. This is carried out in the form of lateral and vertical smoothing , in addition to a small degree of norm damping. The lateral smoothing is applied through the minimization of the spatial gradients of each of the parameters, an approximate to Laplacian smoothing.

For a particular model parameter $\Gamma_i(\theta, \phi, r)$, we minimize the difference between the value of Γ_i at the ith model knot with an average of the nearest neighbour knots Γ_k (where $k \in \forall\, i$ which are the N_i neighbours of i). We note that any particular knot typically has six nearest neighbours, though a small percentage have only five. For example, the ∼280 km grid has 7842 lateral shell knots; of these, 7830 have six neighbours while the remaining 12 have only five neighbours (two of these are the North and South Poles).

For each model knot i, we penalize the difference:

$$\Lambda \varrho(r)\, |w_i \cdot \Gamma_i \; - \; \sum_{k=1}^{N_i} w_i^{\dagger} \cdot \Gamma_k|, \tag{A1}$$

where Λ is the smoothing factor, $\varrho(r)$ is a weight based on the average matrix column-sum for each depth (the purpose of these weights is to prevent over-smoothing at depths where the data sampling is weaker than the maximum sampling), and w_i and $w_i^{\dagger}$ are the weights for the i^{th} model knot and its N_i neighbours (k), respectively. These weights are given by:

$$\begin{aligned} w_i^{\dagger} \; &= \; \frac{1}{N_i + 1}, \\ w_i \; &= \; 1 \; - \; w_i^{\dagger} \; = \; \frac{N_i}{N_i + 1}. \end{aligned} \tag{A2}$$

The imposed lateral smoothing constraint given by eq. (A1) is applied individually to each model parameter A_0, A_1 and A_2, with the aim to reduce spatial variations in the values between the model knot and its neighbours, yielding 'smooth' variations in each of these parameters. For the isotropic velocity (A_0) this regularization is valid globally. However, in the case of the anisotropic terms A_1 and A_2, their independent treatment produces a smooth pattern of each model parameter, but not necessarily of the vector quantity they represent:

$$\underline{a}_i \; = \; \{A_1^i, \; A_2^i\}. \tag{A3}$$

In polar regions where deviations in the local meridian are present, smooth patterns of A_1 and A_2 individually do not necessarily produce a 'geographically smooth' or consistent pattern of anisotropy, $\underline{a}_i$. This breakdown is illustrated by Ma & Masters (2015) (fig. 1 within).

To eliminate effects of the spatially variable local meridian azimuth and more accurately resolve the anisotropic variations in polar regions, we have modified our implementation of lateral smoothing. We utilize a different approach than Ma & Masters (2015),

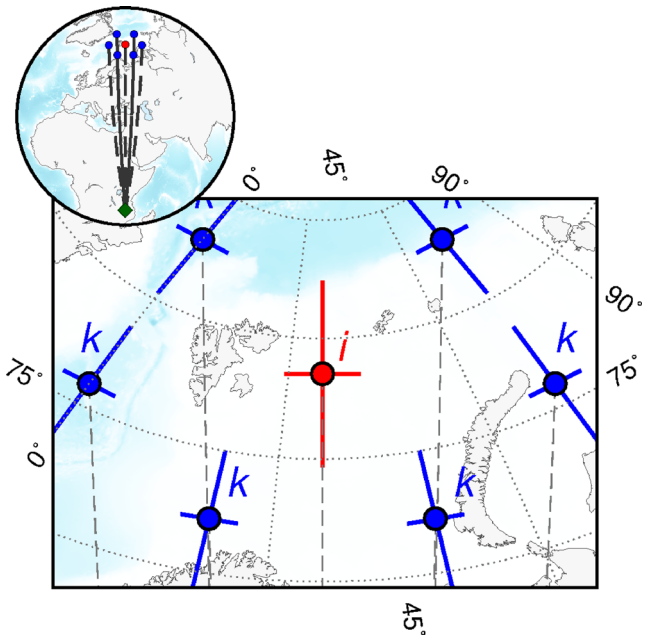

Figure A1. Example model knot (i, red axes) and its six neighbour knots (j, blue axes). Dashed lines connect each of these knots to the reference point $(\theta_i^R, \phi_i^R) = (12°\text{S}, 0°\text{E})$, located 90° south from the model knot at $(\theta_i, \phi_i) = (78°\text{N}, 0°\text{E})$, indicated by the green diamond on the inset. The azimuth of the grey lines at each neighbour knot, ζ_k^R, are used to compute the local meridian correction angle, α_k. Neighbouring knots located west of (θ_i, ϕ_i) have $\zeta_k^R > 0$, whereas those to the east have $\zeta_k^R < 0$.

who apply smoothness constraints in the locally defined North and Northeast directions. We instead choose to minimize locally rotated components of the anisotropy vector:

$$\tilde{\underline{a}}_k \; = \; \underline{\underline{R}}_{kj}\, \underline{a}_j, \tag{A4}$$

where $\underline{\underline{R}}_{ij}$ defines the local re-orientation required for each k neighbour of the ith model knot. Importantly, this rotation maintains the linearity of the smoothing-constraint equations for each of the anisotropic terms. This correction is applied globally, even at grid knots near the equator. The strength of the correction term (degree of rotation required) decreases rapidly away from the poles. As a result, this formulation leaves the anisotropy through the mid-latitudes essentially unchanged, while reducing the bias in polar regions.

We explain the correction using an example near the North Pole. We also note that although the correction is described for the 2Ψ terms, it is directly applicable to the 4Ψ terms as well.

At each model knot the anisotropy vector $\underline{a}_i$ is defined with respect to the local meridian, therefore the orientations of (A_1, A_2) at the neighbour knots do not correspond to those of the model knot. To correct for this, we take an approach similar to that used in mapping each path onto the model grid.

We begin by defining a reference point (θ_i^R, ϕ_i^R) a distance 90° away from the ith model knot; the reference point for knots in the southern hemisphere map to the northern hemisphere and vice versa. We then compute the azimuth ζ_i^R from the model knot (θ_i, ϕ_i) to the reference point (θ_i^R, ϕ_i^R), which is 180° (or 0°) for each (θ_i, ϕ_i) in the northern (or southern) hemisphere. Then for each of the N_i neighbouring knots of i, the azimuth ζ_k^R from the neighbour knot (θ_k, ϕ_k) to the reference point (θ_i^R, ϕ_i^R) is computed.

The azimuths ζ_i^R and ζ_k^R are plotted on Fig. A1 as dashed lines originating at the model knot i (red axes) and its six neighbouring knots k (blue axes), respectively. As the ith model knot here (red)

is located at $(\theta_i, \phi_i) = (78^\circ\text{N}, 0^\circ\text{E})$, the reference point is located at $(\theta_i^R, \phi_i^R) = (12^\circ\text{S}, 0^\circ\text{E})$, which is well south of the limits of this figure.

For each of the k neighbouring knots of i, a local meridian correction term, α_k, is computed as the difference between the two azimuths (ζ_k^R, ζ_i^R) to the reference point:

$$\alpha_k \;=\; \left(|\zeta_k^R| - \zeta_i^R\right) \cdot \text{sgn}\left(\zeta_k^R\right), \tag{A5}$$

where the sgn function returns 1 or -1 depending on the sign of its argument. This correction angle is then used to rotate the axes at the neighbouring knots j to an orientation parallel with the local meridian at i.

The linear smoothness constraints that were independent for each unknown parameter are now coupled for the anisotropic terms. A rotation matrix $\underline{\underline{R}}$ using the angle α_k is defined as:

$$\underline{\underline{R}}_k \;=\; \begin{bmatrix} \cos\alpha_k & \sin\alpha_k \\ -\sin\alpha_k & \cos\alpha_k \end{bmatrix}, \tag{A6}$$

which is then applied to the anisotropy vector at k to produce a set of rotated components:

$$\begin{aligned} \underline{\tilde{a}}_k \;&=\; \underline{\underline{R}}_k \underline{a}_k \\ &=\; \begin{bmatrix} \cos\alpha_k & \sin\alpha_k \\ -\sin\alpha_k & \cos\alpha_k \end{bmatrix} \begin{bmatrix} A_1^k \\ A_2^k \end{bmatrix}, \end{aligned} \tag{A7}$$

with

$$\underline{\tilde{a}}_k \;=\; \{\tilde{A}_1^k,\; \tilde{A}_2^k\}, \tag{A8}$$

where the notation A_1^k is a compact form for $A_1(\theta_k, \phi_k)$ and $\tilde{A}_1^k$ denotes the rotated $A_1(\theta_k, \phi_k)$ term projected onto the meridian of i at each k.

The smoothness constraints for each of A_1 and A_2 are then cast in terms of the rotated anisotropic vector $\underline{\tilde{a}}_k = \{\tilde{A}_1^k,\; \tilde{A}_2^k\}$:

$$\begin{aligned} A_1 \;:\; \Lambda\varrho(r)\,|w_i \cdot A_1^i \;-\; \sum_{k=1}^{N_i} w_i^\dagger \cdot \tilde{A}_1^k|, \\ A_2 \;:\; \Lambda\varrho(r)\,|w_i \cdot A_2^i \;-\; \sum_{k=1}^{N_i} w_i^\dagger \cdot \tilde{A}_2^k|, \end{aligned} \tag{A9}$$

where the weighting terms w_i and $w_i^\dagger$ are the weights as in eq. (A1), and each of the rotated components of the vector $(\tilde{A}_1^k,\; \tilde{A}_2^k)$ are each a linear combination of the original vector at k:

$$\begin{aligned} \tilde{A}_1^k \;&=\; \cos\alpha_k\, A_1^k + \sin\alpha_k\, A_2^k, \\ \tilde{A}_2^k \;&=\; -\sin\alpha_k\, A_1^k + \cos\alpha_k\, A_2^k. \end{aligned} \tag{A10}$$

An example for one of the k neighbours of the ith model knot is illustrated in Fig. A2. It is clear from this figure why the rotated components $\tilde{A}_1^k$ and $\tilde{A}_2^k$ are the more appropriate terms to use in the smoothing around i than the original A_1^k and A_2^k at k.

If the relative angle of rotation between the ith knot and its kth neighbour is zero (i.e. on the same meridian), then $\tilde{A}_{1,2}^k = A_{1,2}^k$. Alternatively, if the kth neighbour lies on the same meridian but translated by 180° longitude (i.e. over the pole), the angle $\alpha_k = 180^\circ$, and therefore $\tilde{A}_{1,2}^k = -A_{1,2}^k$. Finally, if the rotation of the axes is $\pm 90^\circ$, then $\tilde{A}_1^k = \pm A_2^k$ and $\tilde{A}_2^k = \mp A_1^k$.

This formulation is numerically efficient to implement, as the angles α_k and their respective sines and cosines depend only on the model grid, and therefore need to be computed only once. Additionally, the radial dependence of the correction is dropped, as the geometry is the same at each depth. Lastly, since the $(\cos\alpha_k, \sin\alpha_k)$ applied to each neighbour are constant multipliers, the smoothness constraints remain linear and are implemented in the same manner as the isotropic velocity.

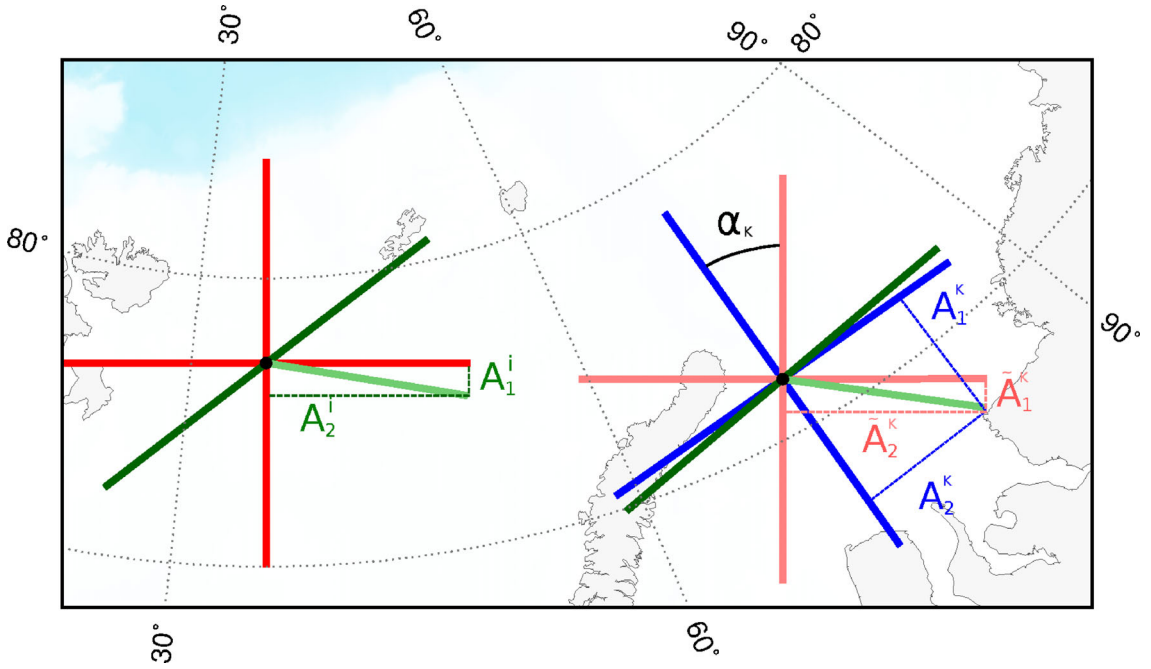

Figure A2. Locally rotated anisotropy vector (light-red axes) at the jth neighbour knot (blue axes), based on its local meridian correction angle α_k with respect to the ith model knot (dark red axes). The orientation of the fast propagation direction is indicated by the green bars, which are continuous (parallel) at both knots. Their corresponding vectors (A_1, A_2) are light-green. The local-rotation angle α_k is indicated at the neighbouring knot, and the rotated projection of the i axes at k are indicated in light red. Each of the A_1 and A_2 components for each set of axes are indicated with their appropriate superscripts.

APPENDIX B: SL2016svA LARGE FORMAT FIGURES

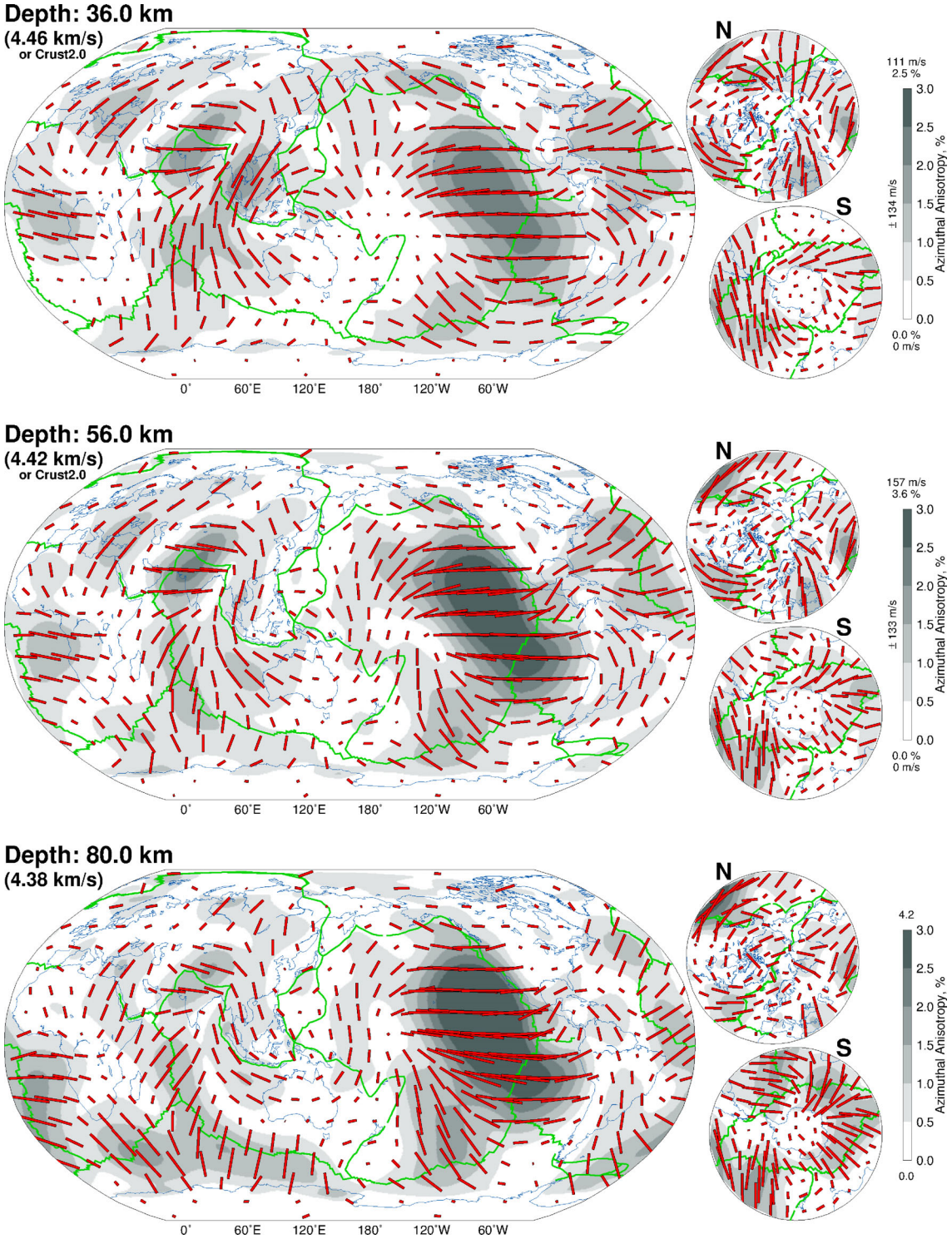

Figure B1. Horizontal cross-sections through SL2016svA, the azimuthal anisotropy component of SL2013sv, at three depths in the shallow upper mantle (and crust in some continental regions). Perturbations in peak-to-peak amplitude are indicated in percent (from the reference V_S, given at the top left of each panel), with the absolute maximum indicated above the scale bar. Because the 36 and 56 km depths are within the crust in some continental regions, with reference S_V values very different from those in the mantle, perturbations are also indicated in m s^{-1}. The yellow sticks reflect the orientation of azimuthal anisotropy re-sampled onto a 5° grid; for the north and south polar views, red sticks are interpolated onto a 500 km triangular grid.

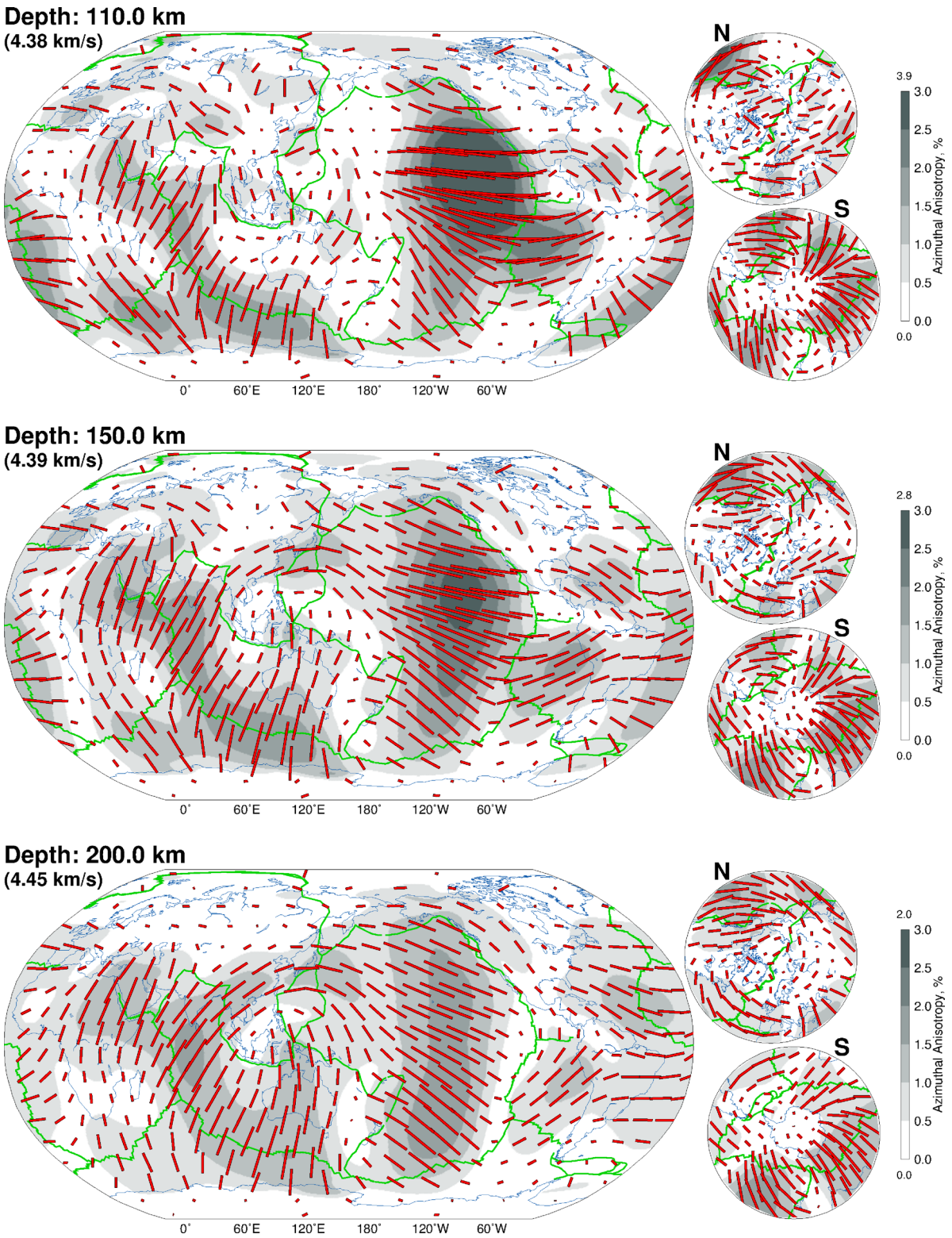

Figure B2. Horizontal cross-sections through SL2016svA, the azimuthal anisotropy component of the tomographic model SL2013sv, at three depths in the lithosphere-asthenosphere depth range. Plotting conventions are as in Fig. B1.

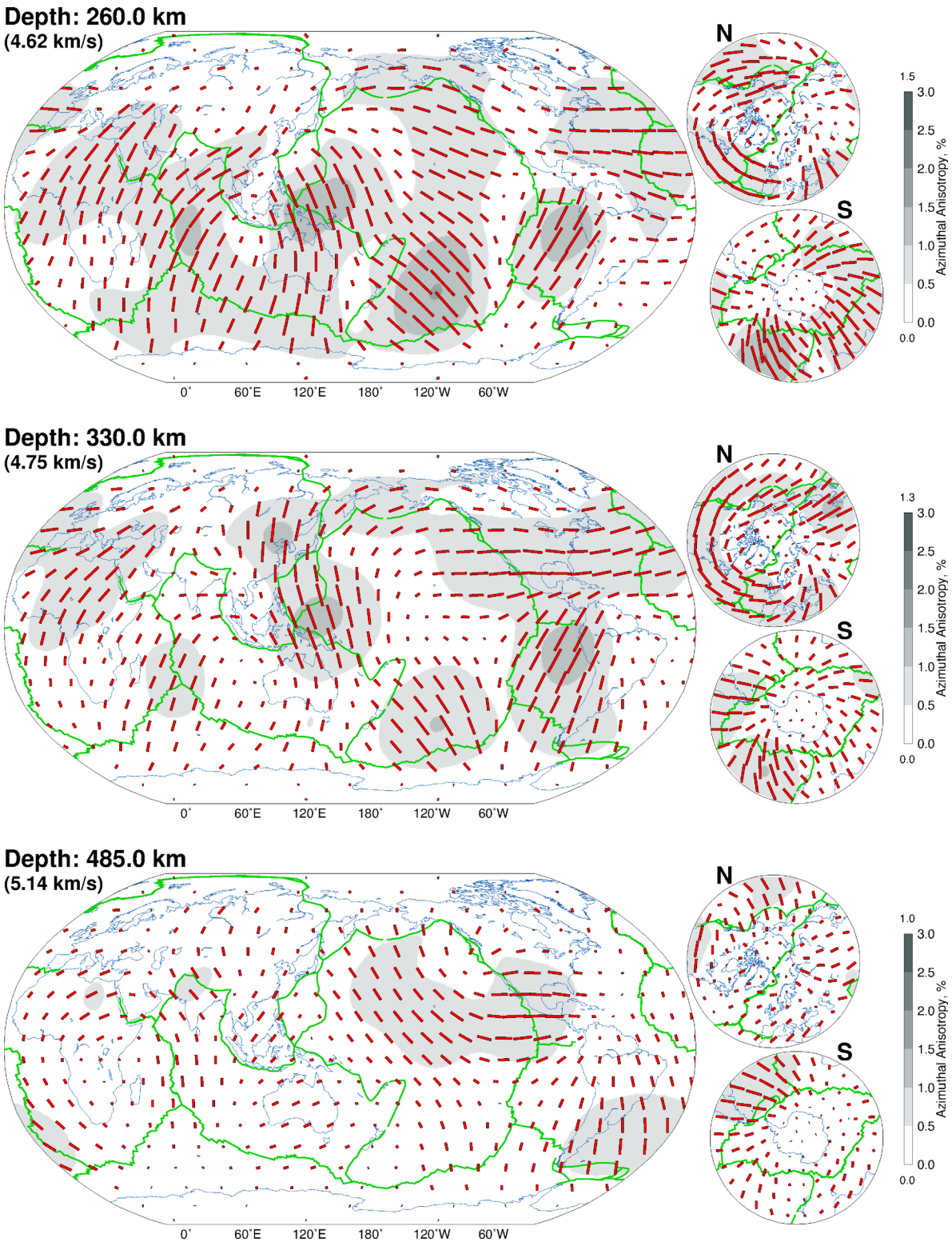

Figure B3. Horizontal cross-sections through SL2016svA, the azimuthal anisotropy component of the tomographic model SL2013sv, at three depths in the deep upper mantle and the transition zone. Plotting conventions are as in Fig. B1.

APPENDIX C: SL2016svAr LARGE FORMAT FIGURES

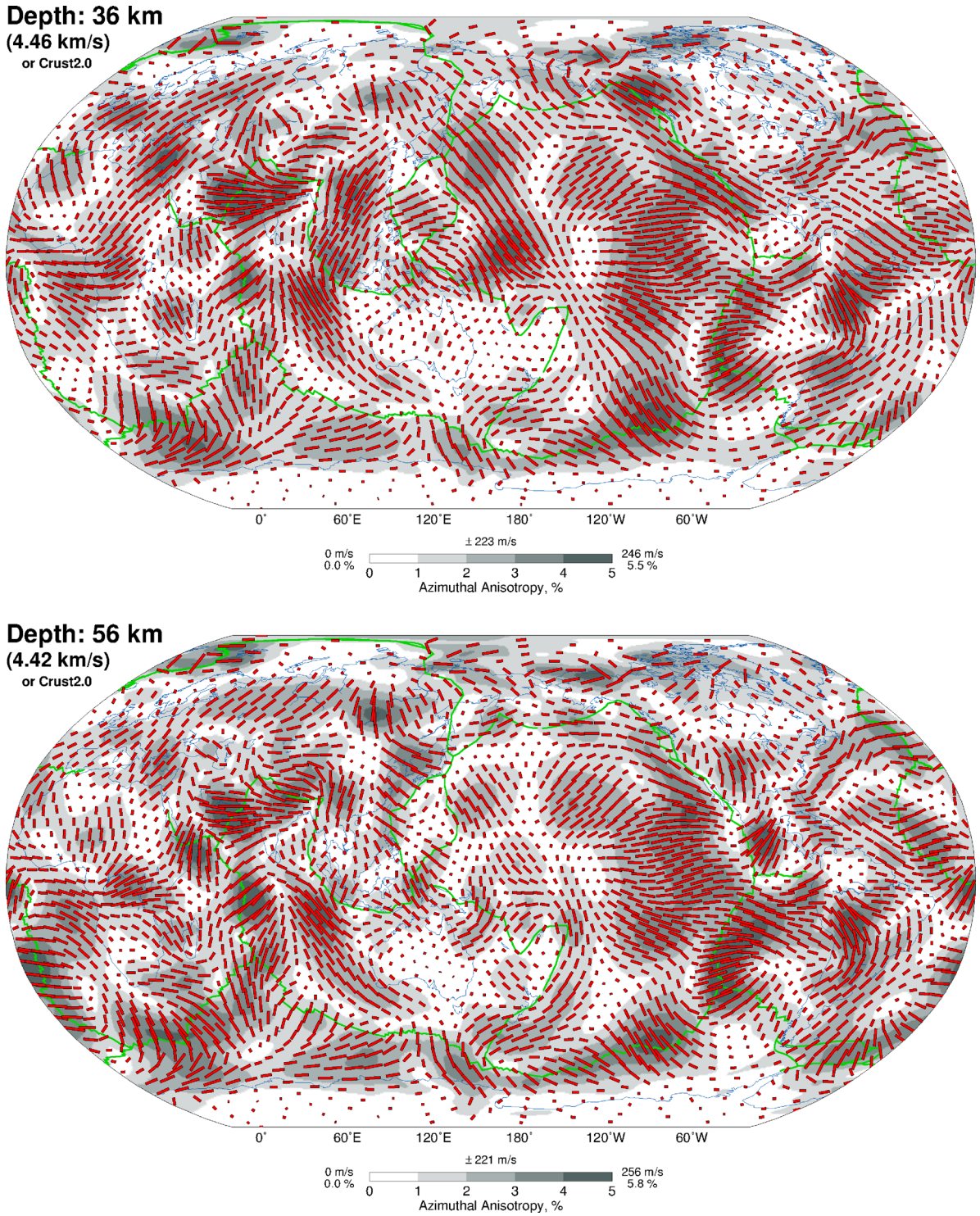

Figure C1. Horizontal cross-sections through SL2016svAr, our rough azimuthal anisotropy model, at two depths in the shallow upper mantle (and crust in some continental regions). Plotting conventions are as in Fig. B1.

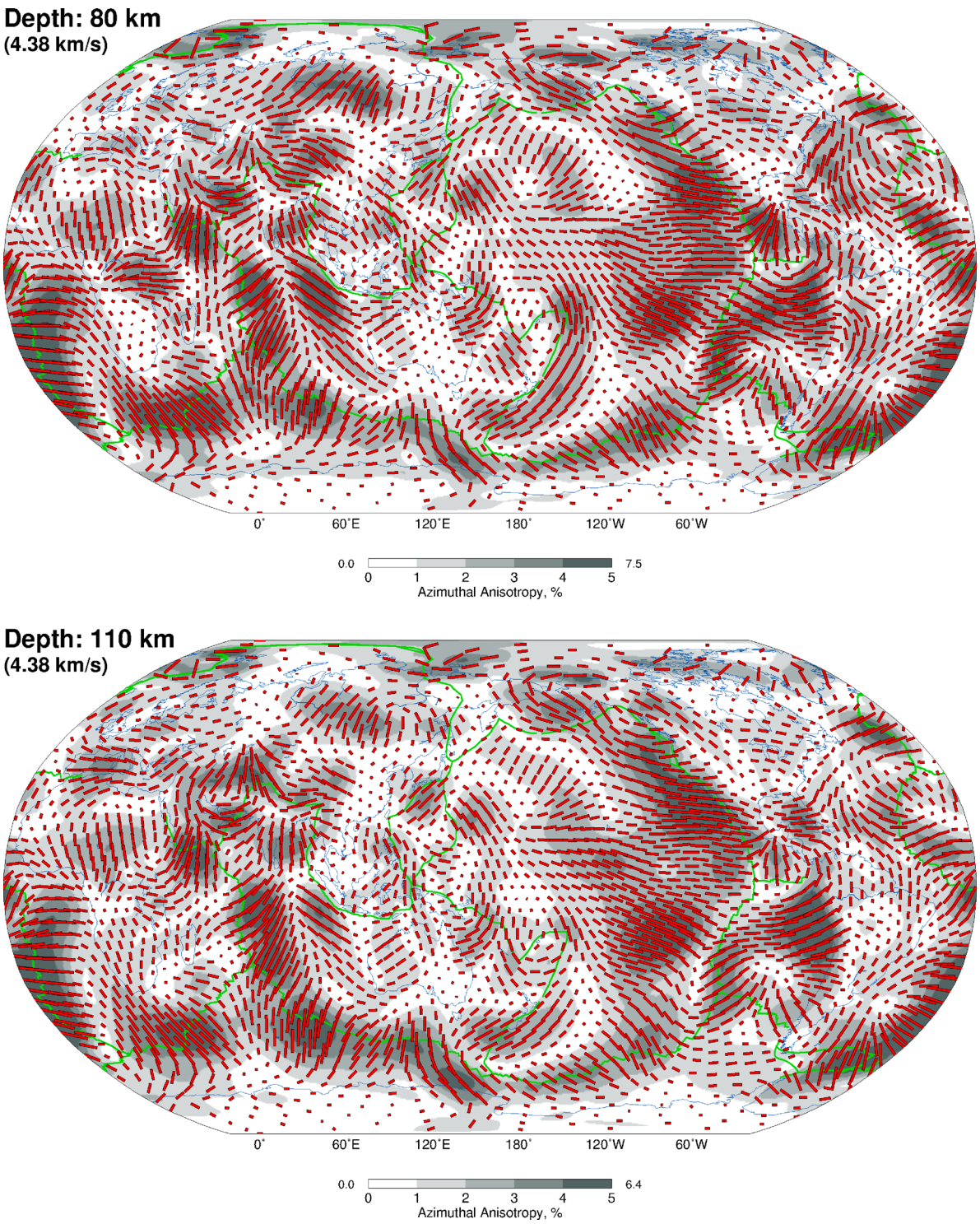

Figure C2. Horizontal cross-sections through SL2016svAr, our rough azimuthal anisotropy model, at two depths in the lithosphere-asthenosphere depth range. Plotting conventions are as in Fig. B1.

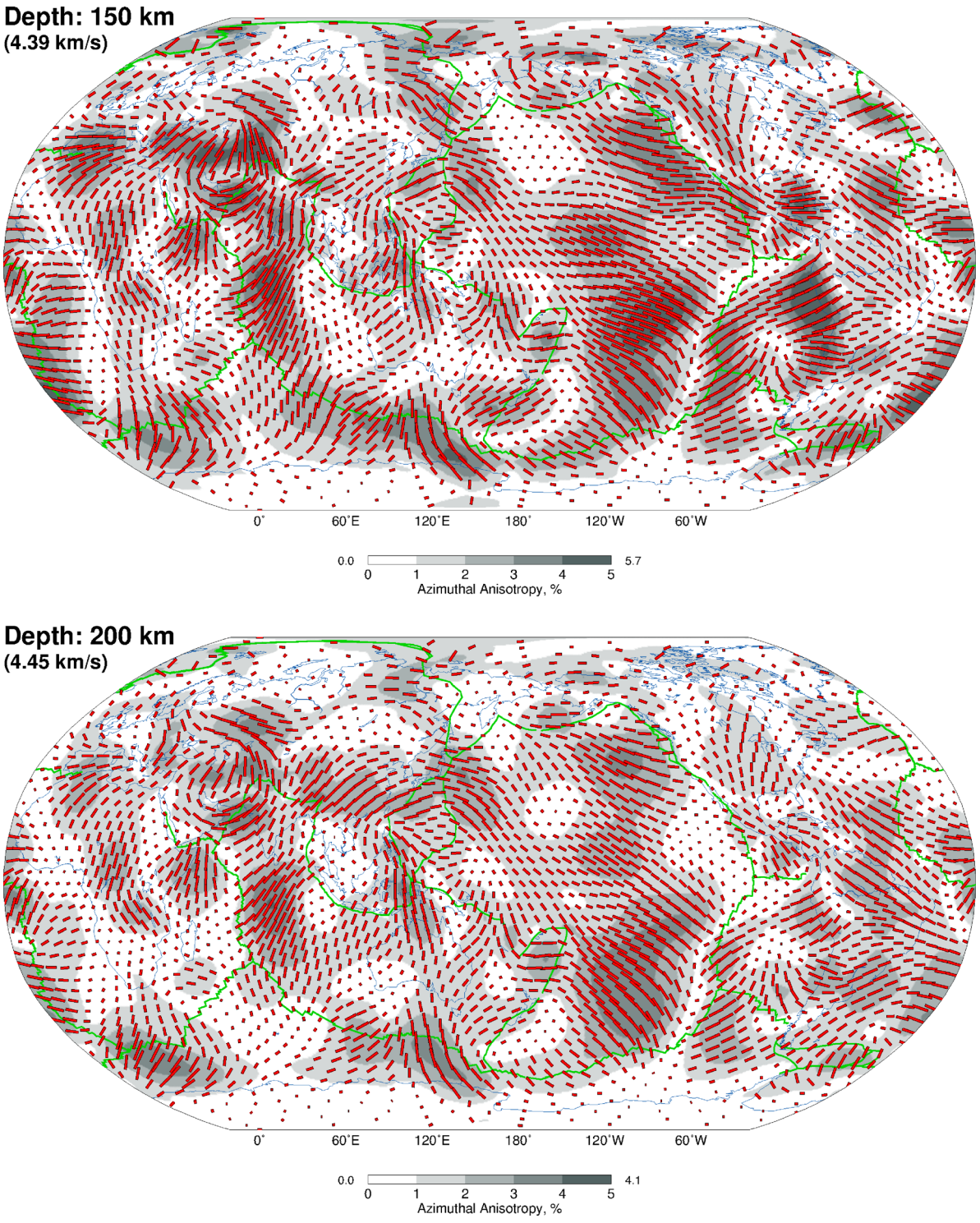

Figure C3. Horizontal cross-sections through SL2016svAr, our rough azimuthal anisotropy model, at two depths in the deep upper mantle and the transition zone. Plotting conventions are as in Fig. B1.

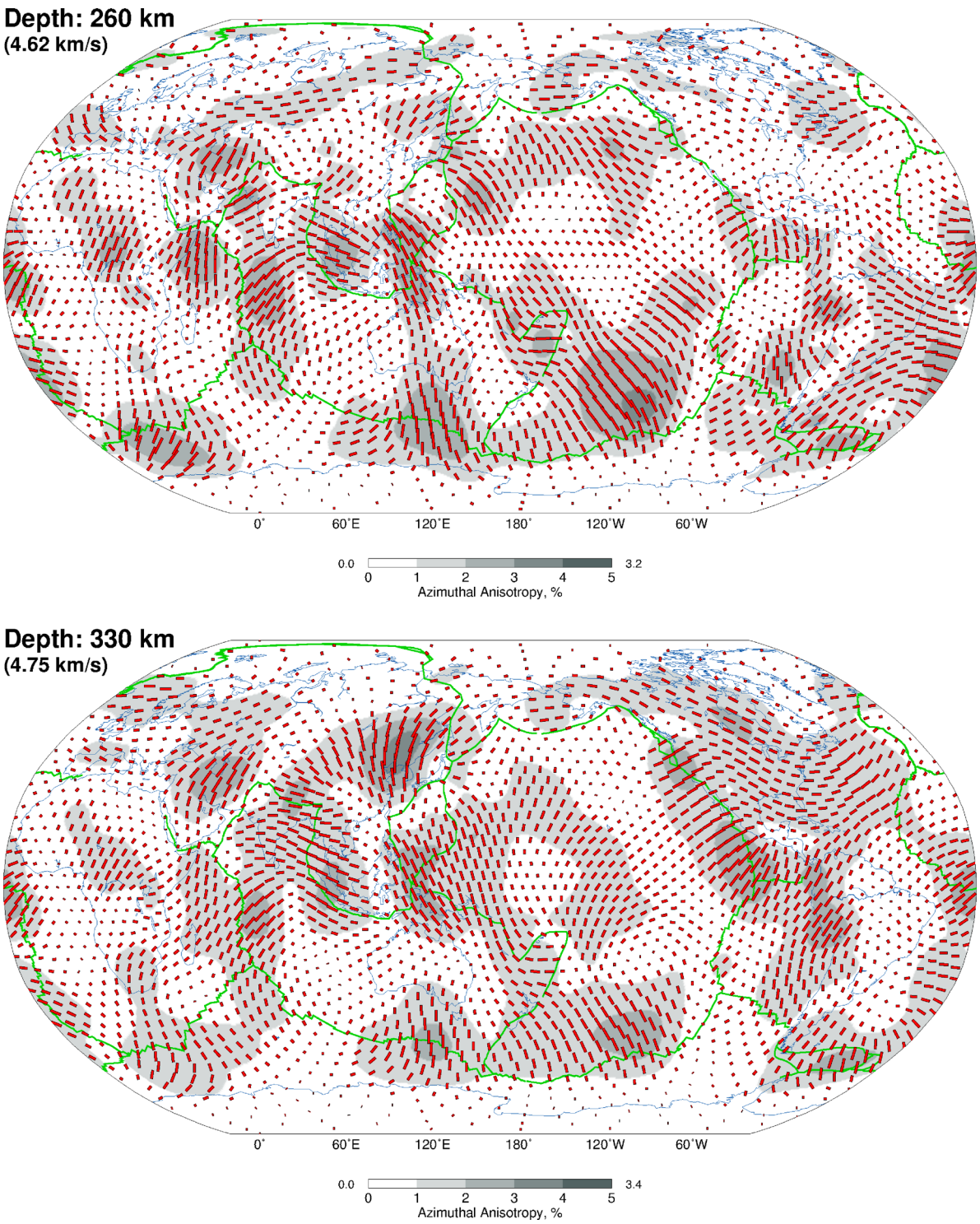

Figure C4. Horizontal cross-sections through SL2016svAr, our rough azimuthal anisotropy model, at two depths in the deep upper mantle and the transition zone. Plotting conventions are as in Fig. B1.

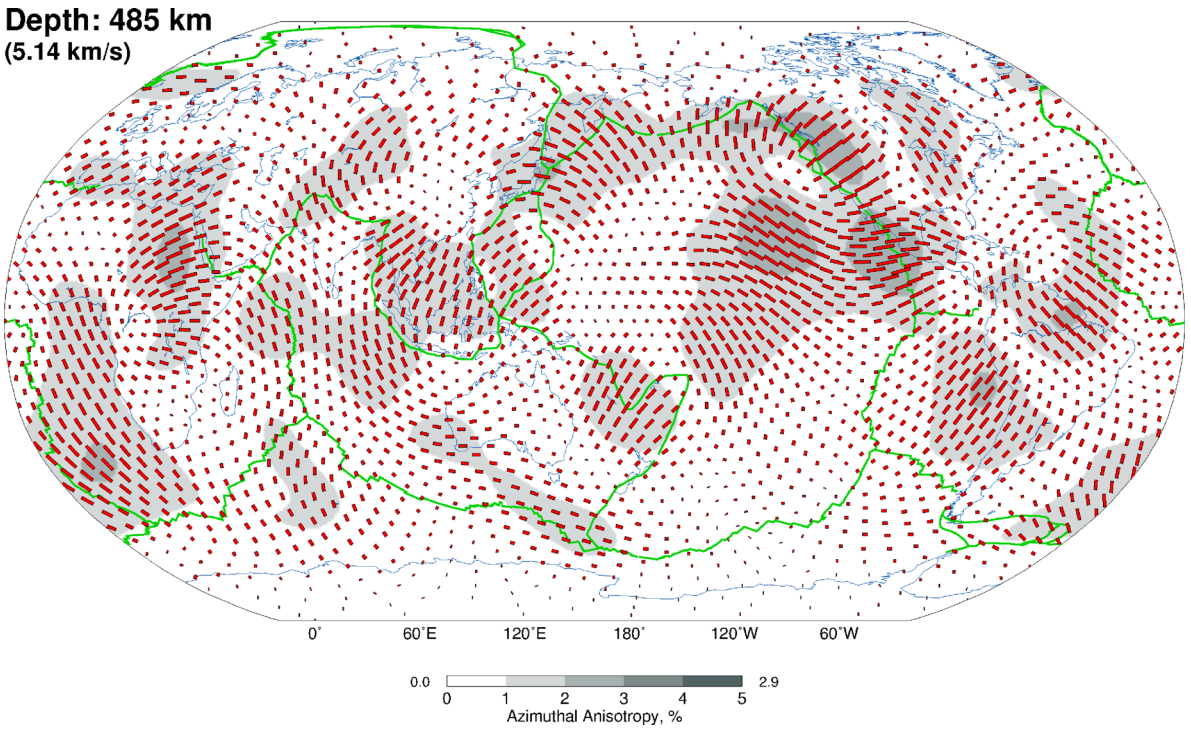

Figure C5. Horizontal cross-sections through SL2016svAr, our rough azimuthal anisotropy model, at a depth in the transition zone. Plotting conventions are as in Fig. B1.